Journal of Volcanology and Geothermal Research 379 (2019) 23–44

Contents lists available at ScienceDirect

Journal of Volcanology and Geothermal Research

journal homepage: www.elsevier.com/locate/jvolgeores

Tecolote volcano, Pinacate volcanic field (Sonora, Mexico): A case of highly explosive basaltic volcanism and shifting eruptive styles

Emily E. Zawacki [a,*], Amanda B. Clarke [a,b], J. Ramón Arrowsmith [a], Costanza Bonadonna [c], Daniel J. Lynch [d,1]

[a] School of Earth and Space Exploration, Arizona State University, Tempe, AZ, USA
[b] Istituto Nazionale di Geofisica e Vulcanologia, Sezione di Pisa, Italy
[c] Département des sciences de la Terre, Université de Genève, Geneva, Switzerland
[d] Department of Geosciences, University of Arizona, Tucson, AZ, USA

ARTICLE INFO

Article history:
Received 7 December 2018
Received in revised form 13 April 2019
Accepted 21 April 2019
Available online 29 April 2019

Keywords:
Tephra deposit
Pinacate volcanic field
Eruptive source parameters
Explosive basaltic eruption
Monogenetic eruptions
Scoria cones

ABSTRACT

Explosive basaltic eruptions have been documented in monogenetic volcanic fields, and recognizing the scales of their explosivity is important for understanding the full range of basaltic volcanism. Here we reconstruct one of the youngest eruptions in the Pinacate volcanic field (Sonora, Mexico) and estimate the volumes of the lava flows, scoria cone, and tephra units. The source vent of the eruption is Tecolote volcano (27 ± 6 ka, $^{40}Ar/^{39}Ar$). There were two distinct episodes of tephra production, Tephra Unit 1 (T1) followed by Tephra Unit 2 (T2). T1 and T2 show different dispersal patterns, with T1 dispersed in an approximately circular pattern and T2 dispersed oblately trending SE and NW of the vent. Based on column height reconstructions and deposit characteristics, the T1-producing eruption was subplinian (15–18 km plume), with a calculated mass eruption rate ranging between $1.0 \pm 0.6 \times 10^7$ kg/s and $2.2 \pm 1.2 \times 10^7$ kg/s and corresponding durations between 79 ± 54 min and 38 ± 26 min, respectively. The T2-producing eruption was violent Strombolian (11 km plume) with a calculated mass eruption rate of $3.2 \pm 1.4 \times 10^6$ kg/s and resulting duration of 193 ± 78 min. In addition to the two tephra units, Tecolote volcano produced seven morphologically distinct lava flows. The majority of lava volume production occurred before—and partly contemporaneously with—tephra production, and five small-volume lava flows were emplaced after pyroclastic activity terminated, indicating shifting and simultaneous eruptive styles. Of the total 0.23 km^3 dense rock equivalent (DRE) erupted volume, the lava flows constitute the majority (0.17 km^3 DRE), with 0.041 km^3 DRE volume for the cone and a combined 0.026 ± 0.005 km^3 DRE volume for the two tephra units. The geochemistry of the samples is consistent with that determined for other Pinacate rocks, which show a trend most similar to that of ocean island basalts and appears characteristically similar to other volcanic fields of the Basin and Range province.

1. Introduction

Basaltic volcanism is the dominant volcanic activity on Earth (Walker, 2000) and can display great variability in eruptive style, ranging from gentle lava flows to explosive magmatic and phreatomagmatic eruptions. These variations in style are in part driven by changes in magma ascent rate, volatile content, and patterns and rates of degassing (e.g., Wilson, 1980; Roggensack et al., 1997; Houghton et al., 1999). Individual basaltic volcanoes can display shifts in—and even simultaneous—explosive and effusive behavior from the same conduit over their lifetime (Valentine and Gregg, 2008), suggesting that their eruptive history may in fact be as complex as that of typical polygenetic volcanoes (Németh, 2010). Although basaltic volcanoes can produce explosive eruptions, highly explosive basaltic eruptions are less well documented and understood than their silicic counterparts (Williams, 1983; Walker et al., 1984; Houghton et al., 2004; Valentine and Gregg, 2008).

While there are relatively few documented cases of large explosive basaltic eruptions, such reconstructed eruptions of the Masaya Caldera Complex, Nicaragua (Plinian – e.g., Williams, 1983; Constantini et al., 2009; Pérez et al., 2009), Tarawera volcano, New Zealand (Plinian – e.g., Walker et al., 1984; Sable et al., 2006), Mount Etna, Italy (Plinian – Coltelli et al., 1998), and Sunset Crater, Arizona, USA (subplinian – Alfano et al., 2018) demonstrate that basaltic systems are capable of producing eruptions on scales typically seen from silicic systems. Understanding the scales of these explosive basaltic eruptions is important when considering hazard assessments for basaltic volcanoes and in investigating the mechanisms that produce these violent eruptions. It is thus important to better understand whether such cases of highly explosive basaltic volcanism are anomalous, or if they are more prevalent than previously thought and should be looked for in the geologic record.

* Corresponding author.
E-mail address: eezawack@asu.edu (E.E. Zawacki).
[1] http://pinacate.org.

https://doi.org/10.1016/j.jvolgeores.2019.04.011
0377-0273/

Pyroclastic deposits are often the only direct evidence of past explosive eruptions, and studying the distribution of the deposit can help characterize the explosivity of the source eruption and associated volcanic hazards (e.g. Bonadonna et al., 2015). Reconstructing eruptive sequences, including the details of explosive eruptions, is an important component in understanding the full range of eruptive styles and transitions between effusive and explosive behavior in basaltic volcanoes (Valentine et al., 2006; Riggs and Duffield, 2008). In any volcanic field, documenting the youngest eruption is important because it is most likely to give clues about the characteristics of the active magma source—both in terms of chemistry and volatile content—and may indicate the type of eruptions to be expected in the future (Harris and Stevenson, 1997; Valentine et al., 2007).

In this paper, we reconstruct the third youngest eruption in the Pinacate volcanic field, Sonora, Mexico. The eruption products include prominent lava flows and two tephra units that extend >10 km from the probable vent—Tecolote volcano (latitude 31.877, longitude −113.362). The sequence represents a wide range of eruption styles, including significant explosive activity. In terms of dispersal area and reconstructed column heights, this eruption is among the most explosive documented eruptions from a basaltic monogenetic scoria cone (Pioli et al., 2008; Alfano et al., 2018). Reconstructing the temporal evolution of the eruption sequence, their individual and combined volumes, and associated eruption rates provides important data for better understanding: (1) transitions between (or simultaneous) eruption styles in basaltic and monogenetic volcanism, (2) the range in explosive eruption scales at mafic volcanoes, including monogenetic fields, and (3) trends in eruptive activity in the Pinacate volcanic field.

2. Geological setting

The Pinacate volcanic field is located in northwest Sonora, Mexico, and comprises a 1500 km^2 area of lava flows with over 400 scoria cones and 8 maars (Gutmann, 2007) (Fig. 1). The field today is part of El Pinacate and Gran Desierto de Altar Biosphere Reserve and is a UNESCO World Heritage Site. Pinacate volcanism is monogenetic and has been intermittently-continuous since initiation in the early Pleistocene (~2 Ma), based on the range of K-Ar ages and variety of cone erosional forms (Lynch, 1981). Dune fields composed of quartzose sand cover 4500 km^2 to the west of the Pinacate (Arvidson and Mutch, 1974). A lower Miocene basalt sequence at 20 Ma and middle Miocene andesite, dacite, rhyolite, and mesa basalt sequence at 15–12 Ma are found to the east of the field (Vidal-Solano et al., 2008).

The Pinacate volcanic field contains two series of lavas: the older Santa Clara series (1.7–1.1 Ma) and the younger Pinacate series (1.2 Ma–12 ka) (Lynch, 1981; Gutmann et al., 2000). The Santa Clara series comprises the trachyte shield volcano Santa Clara (Fig. 1) and is a differentiated basalt-to-trachyte series. The younger Pinacate series contains basalt to hawaiite flows with monogenetic cones (Lynch, 1981). This shift in lava composition thus suggests a shift in magma generation and/or storage conditions beneath the field over time (Lynch, 1981).

Alignment of vents in the Pinacate field exhibits a main N10E trend, likely reflective of the current regional extensional Basin and Range stress regime (Lutz and Gutmann, 1995). Vents younger than ~400 ka are also elongate at N20W and N55W. The N20W control is of unknown pre-Pleistocene heritage, but Lutz and Gutmann (1995) hypothesize

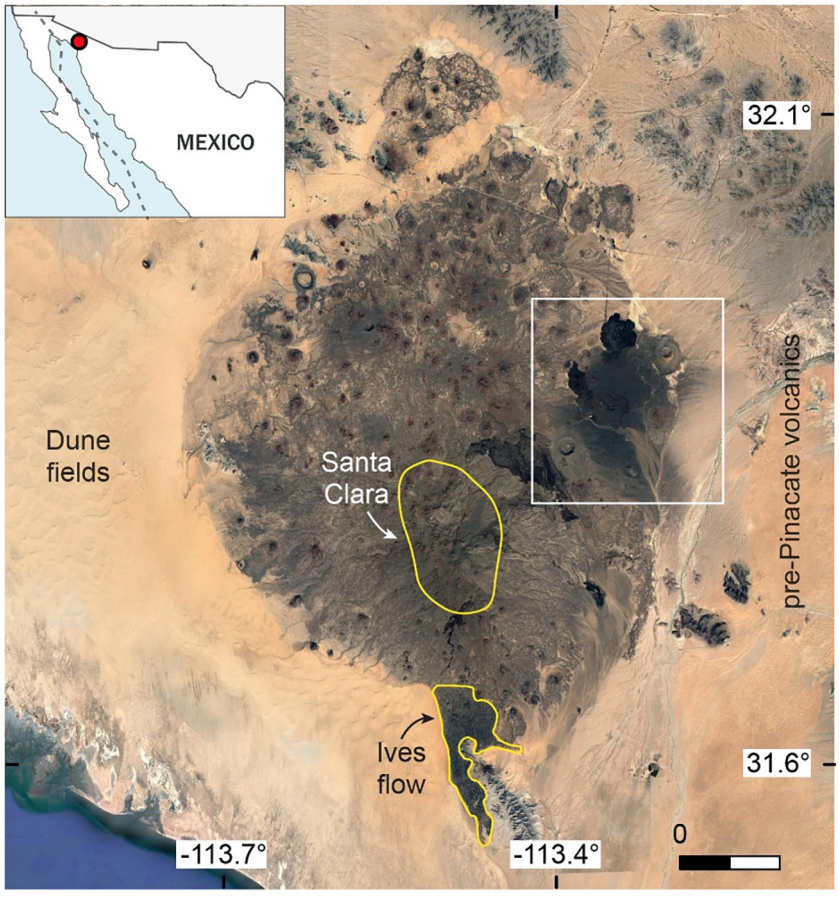

Fig. 1. Geographic location and aerial overview of the Pinacate volcanic field. White box outlines the approximate extent of study area and tephra deposit (Fig. 2). The shield volcano Santa Clara and the Ives lava flow are outlined in yellow. Gran Desierto de Altar dune fields are located to the west of the Pinacate, and pre-Pinacate volcanic rocks are located to the east. Map inset shows Pacific and North American plate boundary with dashed line. (For interpretation of the references to color in this figure legend, the reader is referred to the web version of this article.) *Image from Google Earth.*

that the N55W control may be related to a major regional fracture of that orientation passing through the field. Although volcanism in the Pinacate was coeval with the generation of magmas at the spreading center in the Gulf of California (~100 km west) at ~2–1.5 Ma, there is no clear isotopic evidence for an influence of the Gulf of California opening on Pinacate volcanism (Lynch et al., 1993). Sr and Nd isotope ratios of Pinacate basalts record the presence of an asthenospheric, rather than an enriched lithospheric mantle source (Lynch et al., 1993). Lutz and Gutmann (1995) found no evidence that support a structural control on Pinacate vent alignments either parallel to rifting or to transform directions in the Gulf of California.

Within the Pinacate, its basalt and hawaiite flows are often characterized by megacrysts of labradorite, in addition to phenocrysts of olivine, augite, and magnetite (Gutmann, 1977). No time-dependent variations in types or compositions erupted have been observed among Pinacate series lavas (Lynch, 1981). The scoria cones in the field tend to display a four-stage eruptive cycle, as described by Gutmann (1979): (1) basal lava flows prior to initiation of pyroclastic activity, (2) cone-building eruptions, (3) upwelling of lava and cone breaching, and (4) terminal pyroclastic eruptions. In addition, maar-forming phreatomagmatic eruptions were preceded by Strombolian activity, rather than initiating with phreatomagmatic activity when magma first approached the surface (Gutmann, 2002).

The eastern portion of the field contains the youngest dated cones and is mantled by an extensive tephra deposit that is the primary focus of this study (Fig. 2). Initial field relations suggest the source vent of the deposit to be Tecolote volcano, which is the second youngest dated cone and third youngest dated feature in the field at an $^{40}Ar/^{39}Ar$ age of 27 ± 6 ka (Gutmann et al., 2000). The only younger dated features in the field are the La Laja cone (Fig. 2) with an $^{40}Ar/^{39}Ar$ age of 12 ± 4 ka (Gutmann et al., 2000), and the Ives flow at the southernmost edge of the field (Fig. 1) with an $^{40}Ar/^{39}Ar$ age of 13 ± 3 ka (Turrin et al., 2008). The eastern portion of the field also contains major phreatomagmatic features, including the maar caldera Crater Elegante and the tuff cone Cerro Colorado. Crater Elegante has an $^{40}Ar/^{39}Ar$ age of 32 ± 6 ka (Gutmann and Turrin, 2006), and the Mayo, Solitario,

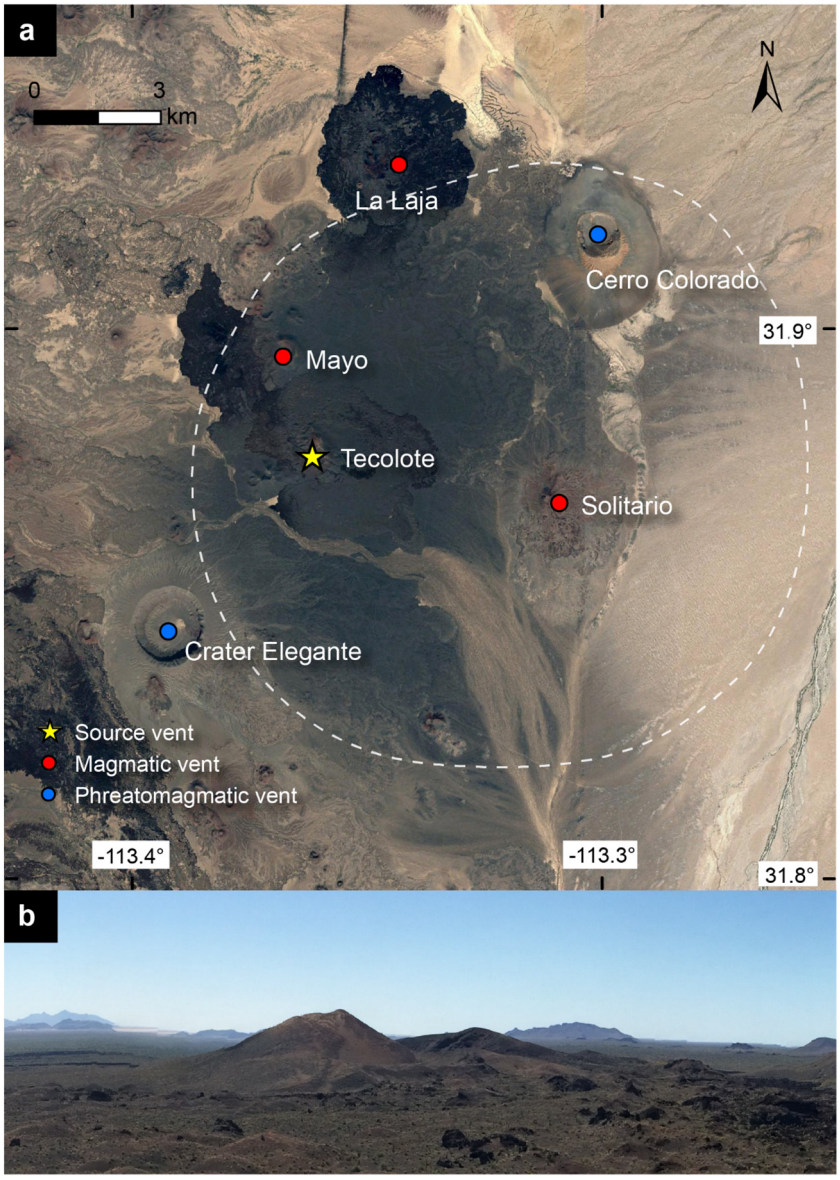

Fig. 2. (a) Eastern portion of the Pinacate volcanic field and study area (white box outlined in Fig. 1). Tecolote volcano (yellow star) is the source vent of the tephra deposit. White dashed line shows approximate extent of tephra blanket. Other features include Crater Elegante and Cerro Colorado (phreatomagmatic vents), and the Mayo, Solitario, and La Laja cones (magmatic vents). *Image from Google Earth.* (b) View toward Tecolote from the north with tephra-covered Q lava flow in foreground (Section 4.3). (For interpretation of the references to color in this figure legend, the reader is referred to the web version of this article.)

and Cerro Colorado cones have Tecolote deposit tephra on their flanks, giving them a minimum age of >27 ka (Gutmann et al., 2000) (Fig. 2).

3. Methods

3.1. Field work and sample analysis

Fifty-five pits were dug across the tephra deposit to describe the stratigraphy, measure unit thickness, and collect samples for sieving and grain size analyses (Fig. 3). Bulk tephra samples were sieved to quantify grain size distribution and sorting. Because the field is part of a Biosphere Reserve, pits were primarily dug near pre-existing unpaved roadways to minimize disturbance. At the same time, significant care was taken to avoid digging pits and sampling in areas that were affected by the unpaved road, passing cars, or any of the washes that pass through the area of the deposit. The eastern portion of the deposit is adjacent to a playa, and little to no primary tephra was identified in that area. The tephra was either removed due to wind erosion and/or buried under playa and aeolian sediments. Due to the heavy deposit reworking and burial here, a portion of the distal deposit can no longer be directly measured.

Across the entirety of the tephra blanket, the top few centimeters of the deposit are heavily infiltrated by dust, which increases in degree of infiltration toward the playa. Tephra clasts on the surface form a desert pavement due to the infiltration of aeolian silts and clays deposited on the land surface (McFadden et al., 1987). The dust infiltration ranges from ~5–30 cm into the uppermost portion of the deposit, which exaggerates the original tephra thickness in the impacted portions. Tephra thickness measurements were made excluding the dust-infiltrated upper portions and are thus minimum bounds on deposit thickness in many sample locations. Measured unit thicknesses were plotted to create isopach maps for deposit volume calculations. In Section 5.1 we estimate the uncertainty in eruption volume introduced by this dust-infiltrated layer.

To create isopleth maps we collected the 5 largest scoria clasts from T1 in 33 pits and from T2 in 13 pits. Each clast was measured across its major and two minor axes. We plotted the arithmetic average of the geometric mean of the three axes of each of the 5 largest clasts. This technique is recommended in the Bonadonna et al. (2018) IAVCEI report examining various maximum clast size averaging techniques. Because we collected only the 10 largest clasts from each pit, we were unable to compare this technique to the method that uses the fiftieth percentile of the 20 largest clasts (Bonadonna et al., 2013). In any case, Osman et al. (2019) has demonstrated that even though the median of a 20-clast population is more representative of outcrop variation, the mean of the 5 largest clasts is a more efficient application to dispersal models, such as those of Carey and Sparks (1986) and Rossi et al. (2019). In addition to isopleth maps, we created isograde maps of median grain size in phi, determined by sieving bulk samples from each location.

We calculated the total grain size distribution of the T1 and T2 deposits using the Biass and Bonadonna (2014) Matlab script, which updates the Bonadonna and Houghton (2005) code for calculating total grain size distributions. This script applies a Voronoi Tessellation method, which calculates the total grain size distribution as the area-weighted average of all the Voronoi cells over the entire deposit. Graphical statistical parameters were calculated following Inman (1952).

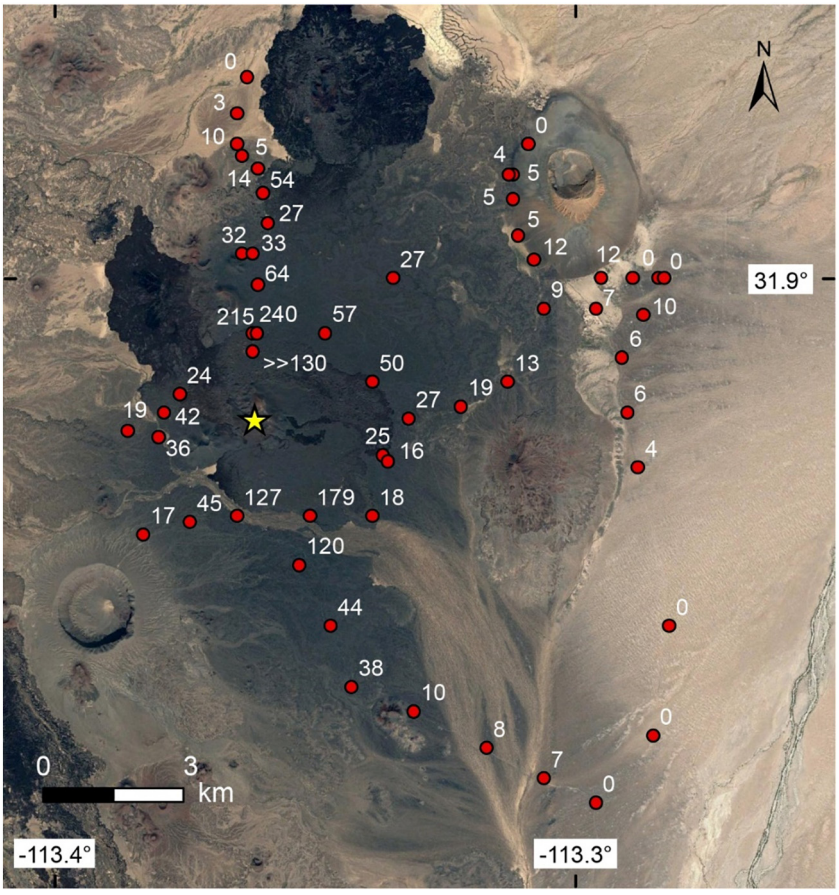

Fig. 3. Location of 55 pits with total combined tephra thickness measured in centimeters (excluding dust infiltration). Largest total thicknesses center around the Tecolote vent (yellow star). (For interpretation of the references to color in this figure legend, the reader is referred to the web version of this article.) *Image from Google Earth.*

3.2. Luminescence dating

To attempt to more tightly constrain the age of the eruption, we collected two samples from the sandy silt unit beneath the tephra deposit for luminescence dating. Luminescence dating methods such as optically stimulated luminescence (OSL) and infrared stimulated luminescence (IRSL) date the last time quartz or feldspar grains were exposed to sunlight by detecting their response to environmental ionizing radiation exposure. Luminescence techniques can date the deposition of sediments back to 200 ka (Rhodes, 2011), which safely brackets the anticipated deposit age. The sandy silt units are in direct contact with the overlying tephra and should provide a maximum age constraint on tephra deposition. Samples were collected in opaque PVC tubes to ensure material had no exposure to sunlight and were sent to the Utah State University Luminescence Laboratory for analyses.

4. Field data and geochemistry

4.1. Luminescence dates

OSL dates from quartz grains yielded a wide range of ages from ~4–40 ka. Quartz in volcanic settings has been found to produce OSL age underestimates due to low OSL emissions (Fattahi and Stokes, 2003; Lian and Roberts, 2006), thus likely making these dates unreliable. IRSL dating of feldspars provided more consistent results. The two IRSL samples yielded ages of 41.8 ± 12.7 ka and 46.4 ± 14.7 ka (2σ error). These dates are both within error of the 27 ± 6 ka $^{40}Ar/^{39}Ar$ date of Tecolote from Gutmann et al. (2000), although their bounds skew significantly older. Given that these ages date the sandy silt unit directly below the tephra rather than the tephra itself, the ages are consistent with the stratigraphy.

4.2. Tephra stratigraphy and grain size characteristics

Stratigraphic descriptions reveal two distinct tephra units (Fig. 4). Tephra Unit 1 (T1) underlies Tephra Unit 2 (T2), is found distributed across the full extent of the deposit, and is roughly circular in map view with a ~6.5 km radius centered on a point directly east of the vent based on the 5 cm thickness contour. Both units are dominated by coarse ash to medium lapilli scoria. We distinguish T1 from T2 based on its distinct, darker color, slightly higher vesicularity, and lack of vertical variations in dominant grain size (fining/coarsening). T2 is distributed oblately around the Tecolote vent extending to the SE (~9.5 km major axis, ~4.5 km minor axis, with respect to the 15 cm thickness contour). T2 coarsens upward and in many sites contains multiple bands of fines near the top. There are no soil or dust layers between T1 and T2 that would indicate a significant gap in time between their emplacements. Southeast of the vent, the contact between T1 and T2 is expressed as a fine-grained ash-rich layer of alternating light-dark-light lapilli scoria.

The tephra deposit commonly overlies an indurated sandy silt layer a few centimeters thick. Below this basal contact, characteristically there is either loose sandy silt, older reworked tephra units, or older basalt flows. Older reworked tephra units were identified based on this indurated basal contact as a distinct break in time, and because they have an overall more weathered appearance. OSL/IRSL samples were collected from the underlying loose sandy silt unit. Southeast of the Tecolote vent, the older tephra deposits appear to have been fluvially reworked with interbedded sand-sized lithic grains. To the east of the vent, T2 is absent and the T1 tephra is overlain by a thin, reworked tephra layer. This overlying tephra layer is light gray in color, consists of rounded fine lapilli, and was interpreted to be distinct from T2 based on differences in major element geochemistry (see Section 4.4). Based on its appearance in outcrop (rounded grains, lamination, thinning trend from east to west), this unit was interpreted to be reworked rather than a primary tephra deposit, either derived from distal portions of T1 or other units sourced from vents to the east of Tecolote.

Stratigraphic columns along north, east, and south transects from the vent highlight the different dispersal trends of T1 and T2 (Fig. 5). In all transects, T1 gradually thins and becomes finer, with the highest degree of sorting in the proximal zone. The unit generally does not display any vertical variations such as fining or coarsening. T2 displays substantially different dispersal trends. In the north and south transects (Fig. 5a and c), T2 is very thick nearest to the vent and then rapidly thins with distance from the vent. In transects directly east of the vent (Fig. 5b), T2 is entirely absent. Stratigraphic sections east of the vent are the only ones that exhibit reworked tephra above T1. Where T2 is present to the north and south, it is fine lapilli at the base and coarsens upward. Southeast of the vent (Fig. 5c), there is a ubiquitous thin ash-rich lapilli scoria sequence between T1 and T2.

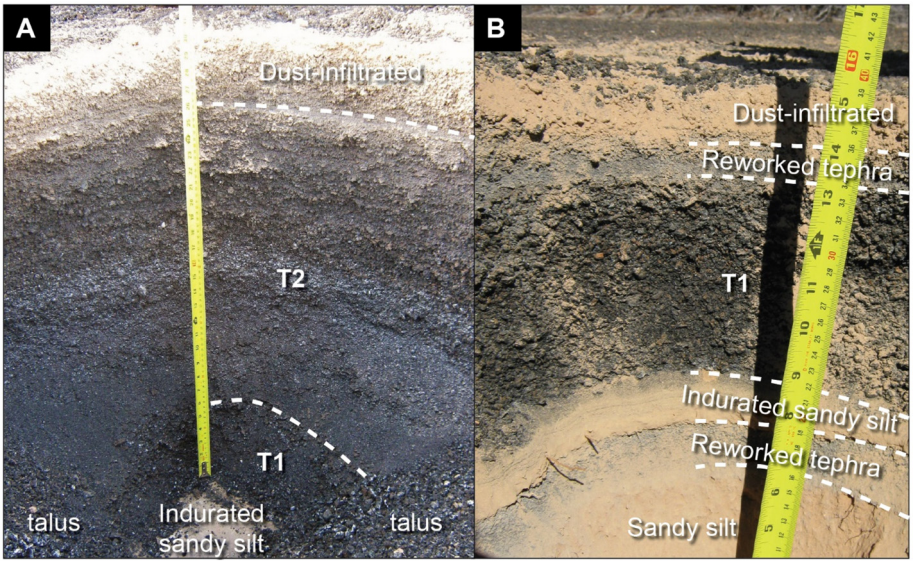

Fig. 4. Example stratigraphy of the tephra deposit in two pits. (A) Pit 2.4 km directly north of the Tecolote vent. Here T2 is five times thicker than T1. T2 is fine at the base and coarsens upward. (Pit 20161207-7). (B) Pit 4.6 km directly east of the Tecolote vent. Here only T1 is present. A reworked tephra directly overlies T1. (Pit 20161113-1).

Isopach maps for T1 and T2 display substantially different contour patterns (Fig. 6). T1's maximum measured thickness was >50 cm, and the largely circular contours are centered east of the vent, with the 5-cm contour extending ~11 km east of the vent (Fig. 6a). T2's pattern is elongated predominantly SE of the vent, although it is also elongated to a lesser extent to the NNW (Fig. 6b). Relative to T1, T2 covers a smaller area but has significantly greater maximum thicknesses of >150 cm. T2 thicknesses rapidly drop off to the east and west of the vent.

Isopleth maps of T1 and T2 (Fig. 7) show similar patterns to the isopach maps. T1's isopleth contours are roughly circular, with its center shifted to the east of the vent (Fig. 7a). T2 again shows elongate isopleth contours trending SE of the vent, with larger maximum clast sizes than T1 (Fig. 7b). Isograde maps of median grain size in phi are shown in Fig. 8 and are consistent with patterns seen in the isopach and isopleth maps.

The grain size characteristics of T1 and T2 are shown in Figs. 5 and 7–10. The deposits are moderately well-sorted and plot in the grain size and sorting field typically associated with fall units (Fig. 9; Walker, 1971). T2, as seen in the north and south transects (Fig. 5a and c), fines to the north and to the southeast, and become slightly more poorly sorted. T1 follows a similar pattern in all directions, although its peak grain sizes tend to be coarser grained than T2, as is most evident in the north transect.

Despite their different vertical fining/coarsening trends, histograms of the total grain size distribution (TGSD) for T1 and T2 show notably similar patterns (Fig. 10). T1 has a median phi grain size (Md_ϕ) of −1.7, and T2 has a Md_ϕ of −1.8. T1 and T2 are similarly moderately well-sorted, with similar degrees of positive skewness and normal kurtosis (Table 1).

4.3. Lava flows and cone

In addition to the two tephra units, Tecolote volcano has seven morphologically distinct lava flows: flows, A, B, C, Q, R, S, and T (Fig. 11;

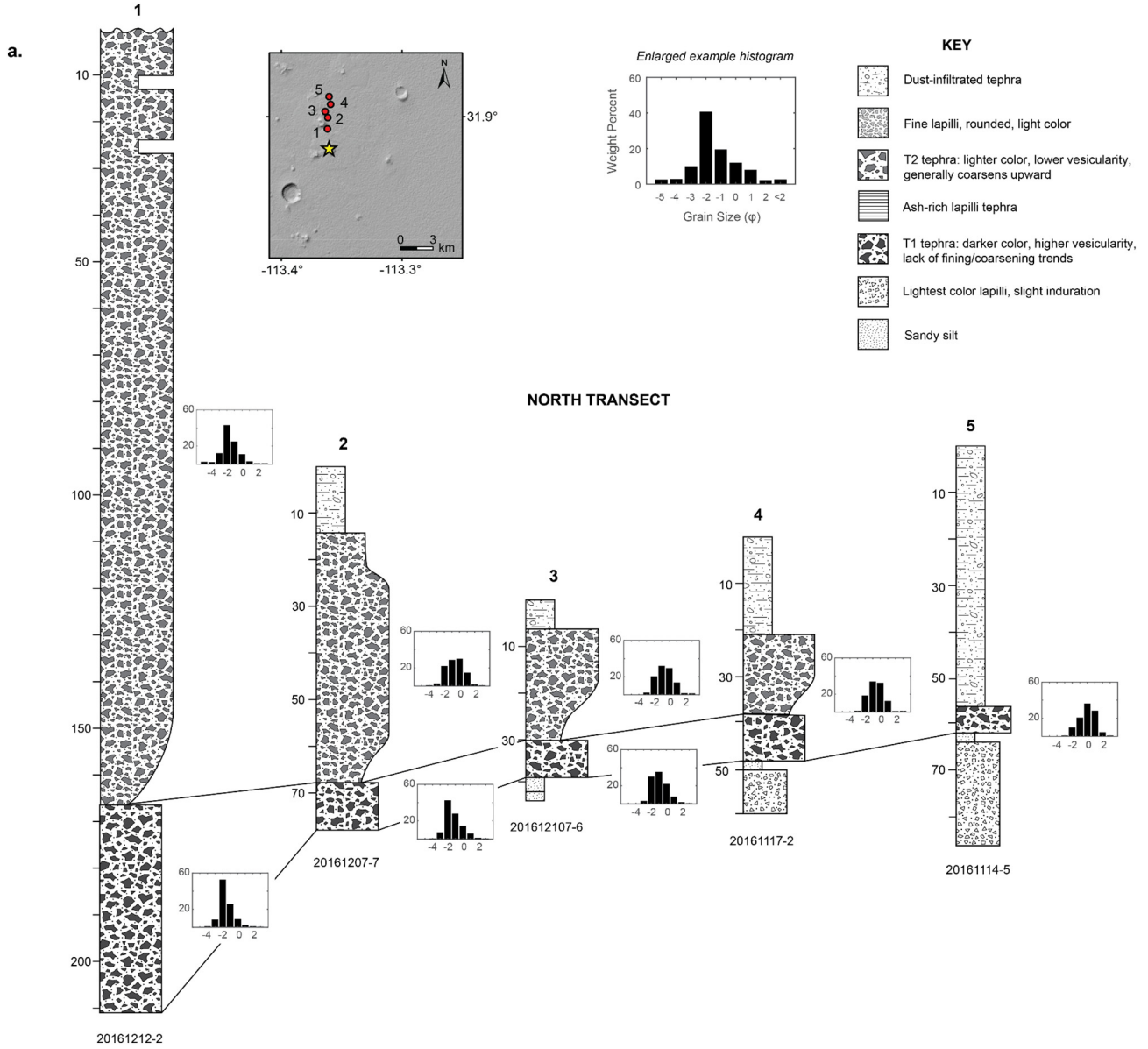

Fig. 5. Transects of stratigraphic columns (a) north, (b) east, and (c) and south of the Tecolote vent. Map inset shows location of sections relative to Tecolote vent (yellow star). Sections also include histograms of grain size distributions where bulk samples were collected. Site numbers appear below each stratigraphic column Legend shows stratigraphic descriptions and enlarged example grain size histogram.

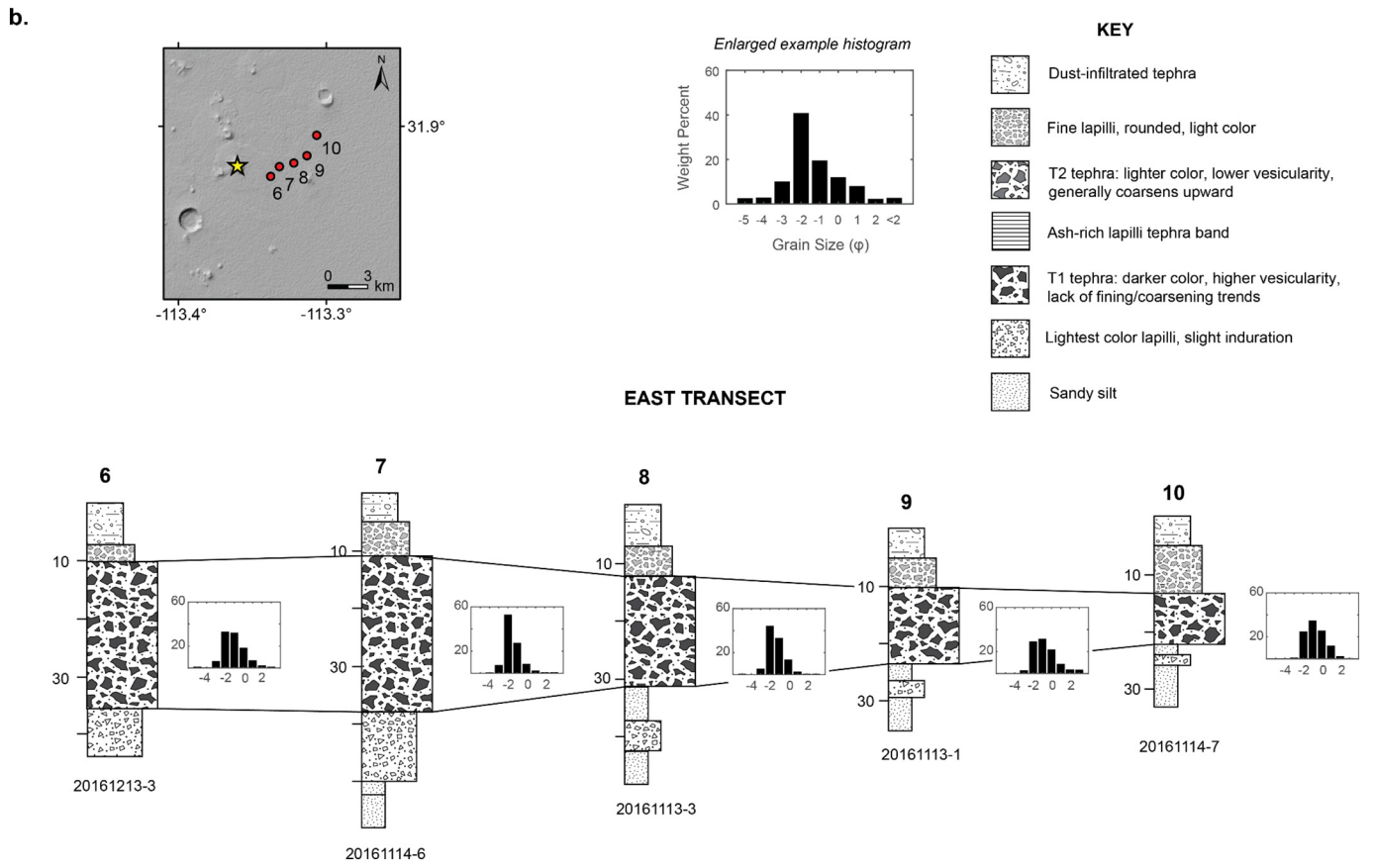

Fig. 5 (*continued*).

Lynch, 1981; Lynch and Gutmann, 1987). The Q flow to the north is the most extensive covering 5.35 km^2 and is almost entirely mantled by tephra. The S flow to the south covers 5.02 km^2 and is covered with tephra on its eastern portion but is tephra free on a small portion of its western tip. Flows A, B, C, R, and T are comparatively small (each <0.15 km^2 in area) and overlie the tephra blanket (Fig. 11a). Based on their field relations, we chronologically group the Q and S flows as Group 1 lavas, the R and T flows as Group 2 lavas, and the A, B, and C flows as Group 3 lavas.

A high-resolution topographic model of the Tecolote edifice and adjacent lava flows from Scott et al. (2018) highlights the complex nature of the Tecolote structure (Fig. 12). The northwest section of the main edifice is fully breached, and there are numerous large rafted portions of edifice material found on the northern Q flow (Fig. 13). There are several well-preserved conical vents seen near the center of the structure, one or more of which could be the source of the tephra sequence and bombs. Three are aligned NE but the overall trend of the vents and breach is NNW. The southern exterior wall is littered with bombs of various sizes that range up to ~2 m in diameter (Fig. 14). Numerous concentric fractures cut through the main edifice, which are particularly apparent on the east and south walls. The limited tephra cover on the fractures suggests that this faulting was a later stage development.

4.4. Geochemical analyses

Lava samples were collected from all seven of Tecolote's lava flows for X-ray fluorescence (XRF) and inductively-coupled plasma mass spectrometry (ICP-MS) major and trace element geochemical analyses (Figs. 15 & 16, Table 2). A Tecolote bomb sample, tephra from T1 and T2 (Fig. 11a), and scoria from the La Laja cone (Fig. 11b) were also collected for analyses. The scoria sample from La Laja was included to determine if it is geochemically distinct from the tephra samples, as La Laja is the youngest dated cone in the field at 12 ± 4 ka (Gutmann et al., 2000). In addition, we collected two samples of the reworked tephra found above T1 east of the vent to assess whether it was related to the T2 tephra (Fig. 11b). Samples were analyzed using XRF and ICP-MS techniques at the GeoAnalytical Laboratory at Washington State University.

In terms of total alkalis and silica, the Tecolote samples are all alkali basalt and the La Laja scoria is a basaltic trachy-andesite. These data are consistent with the basalt to hawaiite compositional range determined for other Pinacate rocks (Lynch, 1981).

Harker diagrams of major element data geochemically characterize the eruptive sequence and demonstrate that the La Laja sample is distinct from all the Tecolote samples (Fig. 15). The La Laja scoria has a significantly higher SiO_2 content (52.7 ± 0.2 wt%, 2σ) than all Tecolote samples (48.1–48.9 ± 0.2 wt%). A diagram of FeO vs. SiO_2 shows a general trend of decreasing FeO through the Tecolote sequence with a large jump to the La Laja sample (Fig. 15a). The K_2O vs. SiO_2 plot reveals a generally increasing K_2O trend through the Tecolote sequence, again with a large jump to the La Laja sample (Fig. 15b). These data further support the conclusion that La Laja did not contribute to the observed tephra deposit and that Tecolote is the source vent of both tephra units.

Tephra from T1 and T2 have different geochemical signatures. While T1 and T2 overlap in SiO_2 within 2σ, they are fully distinct in their TiO_2, MnO, CaO, Na_2O, and K_2O values (Table 2; Fig. 16). These data support two distinct episodes of tephra production from Tecolote volcano. The bomb sample shows the closest relationship to the T2 tephra, suggesting that it was connected to the final explosive stage. In addition, the tephra found above T1 east of the vent is geochemically distinct from

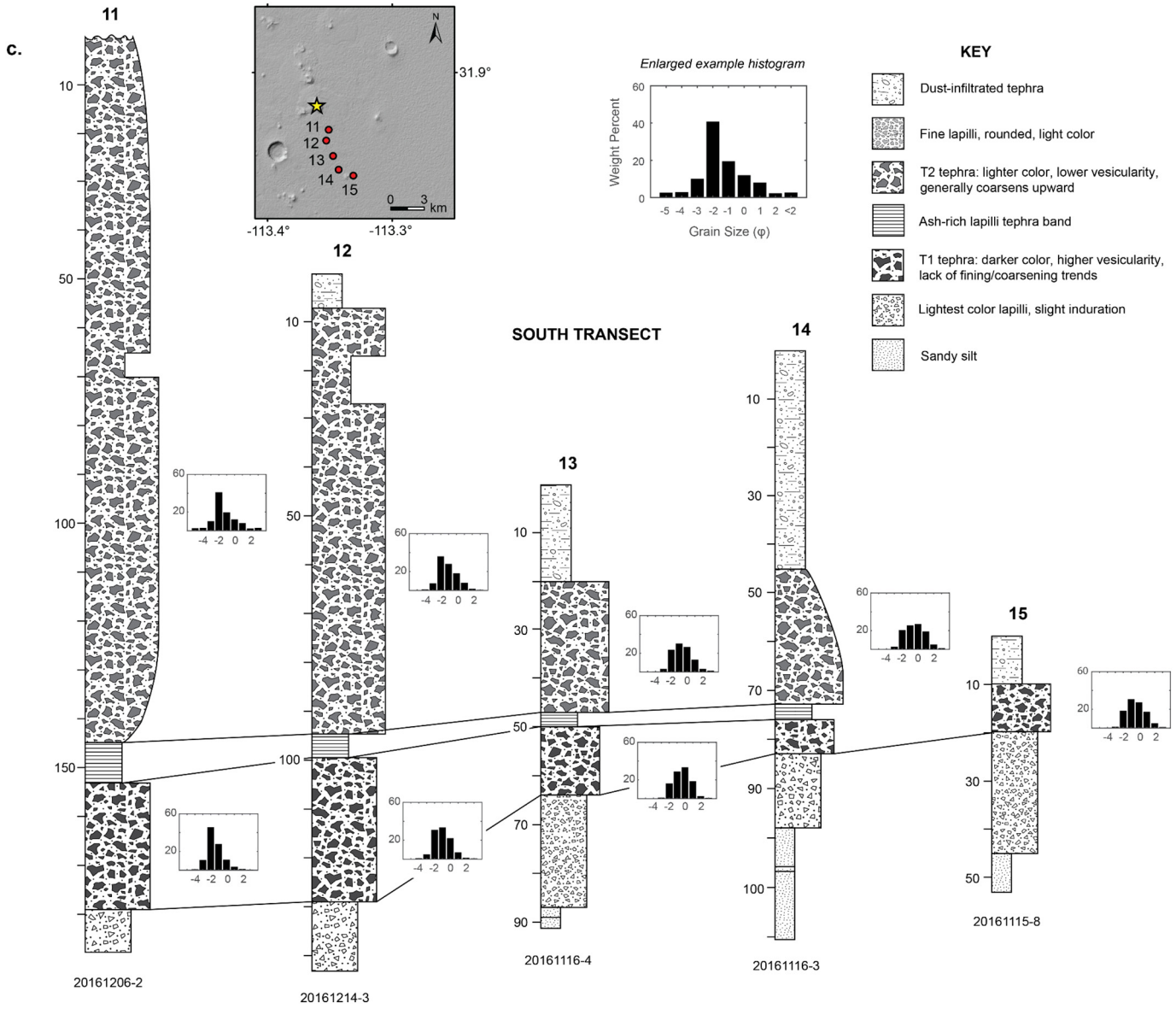

Fig. 5 (*continued*).

T2 (Fig. 15b). This tephra is most similar in SiO_2 and other major elements to the T1 signature (Table 2) and thus could be a layer of reworked material derived primarily from T1. Alternatively, the unit could be partially or wholly derived from reworked tephra from vents to the east of Tecolote, although eruptions from vents to the east are older than Tecolote and tend to be tephra-poor.

FeO, K_2O, and CaO data on Harker diagrams most clearly display a geochemical sequencing in the lava samples (Fig. 16). FeO and CaO weight percent decreases over the inferred sequence, while K_2O increases over the same sequence. The final tephra-producing episode must have been contemporaneous with terminal Q flow and S flow emplacement, as the majority of these flows are covered with tephra, but the western edges of the flows are notably depleted of or devoid of tephra cover. The tephra from T2 in a pit dug on the Q flow was oxidized and deeply red in color, suggesting that tephra was deposited while the lava was still hot. We were unable to dig deep enough on the Q flow to determine whether or not both T1 and T2 overlie it. After tephra deposition, the small flows R, T, A, B, and C were then emplaced, which range in SiO_2 content from 48.3–48.6 ± 0.2 wt%. Within the bounds of the SiO_2 2σ values, the silicic evolution of the flows cannot be resolved.

On a spider diagram of whole rock normalized to primitive mantle (Fig. 17), the Pinacate samples most closely follow an ocean island basalt (OIB) trend. These trace element data are in agreement with the Lynch et al. (1993) Sr and Nd isotope data of Pinacate basalts which record the presence of an asthenospheric rather than an enriched lithospheric mantle source.

5. Results and analysis: eruption reconstruction

5.1. Tephra volume estimates

To determine deposit volumes, the area of each isopach contour (Fig. 6) was measured in ArcGIS, and the square root of each contour area was plotted against deposit thickness on a semi-log plot (Fig. 18). Volumes were calculated based on the integration of: Weibull best-fit (Bonadonna and Costa, 2012), exponential best-fit (Fierstein and

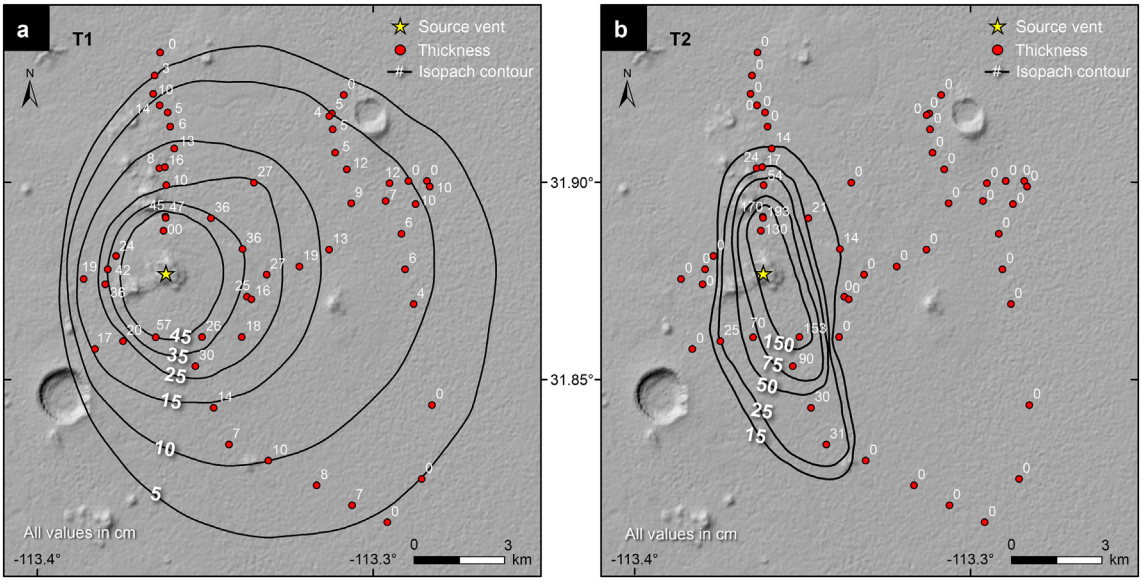

Fig. 6. Isopach maps in centimeters for (a) T1 and (b) T2.

Nathenson, 1992; Nathenson, 2017), and power-law best-fit (Bonadonna and Houghton, 2005). For power-law calculations, a distal integration limit ranging from 40 to 50 km (area$^{1/2}$) was chosen for T1, and for T2 a range of 18–25 km was chosen. These values were based on where thickness extrapolations reached ~1 cm.

We determined an average deposit density of 757 ± 61 kg/m^3 for T1 and 894 ± 108 kg/m^3 for T2, based on five in situ measurements of T1 and seven of T2. We collected and weighed a 2 L volume of bulk material for each density measurement. In order to convert eruption volumes to dense rock equivalent (DRE) volumes, we assume a DRE value for an alkali basalt to be 2700 kg/m^3.

The volume of T1 based on the Weibull best-fit was calculated to be 4.3×10^7 m^3 (DRE $1.2 \pm 0.1 \times 10^7$ m^3). On a semi-log plot of thickness against area$^{1/2}$, the Weibull best-fit shows a similar trend to the exponential best-fit (Fig. 18a), which yielded a deposit volume of 3.9×10^7 m^3 (DRE $1.1 \pm 0.1 \times 10^7$ m^3). While the Weibull and exponential best-fits yielded relatively similar values, the integration of the power-law fitting yielded a significantly higher deposit volume of $6.4 \pm 0.5 \times 10^7$ m^3 (DRE $1.8 \pm 0.2 \times 10^7$ m^3) (Table 4). The power-law best-fit of the T1 data yielded a power-law exponent of ~1.5 (Table 3), suggesting that this technique may be associated with large uncertainty for this deposit. In fact, the power-law fit can better reproduce the natural thinning of tephra deposits, but it can overestimate the volume when proximal or distal data are missing depending on the specific power-law exponent (Bonadonna and Houghton, 2005; Bonadonna and Costa, 2012). In this deposit, the distal edges of T1 are adjacent to a playa and have largely been eroded away or buried. Bonadonna and Houghton (2005) also note that the integration of the power-law fit is

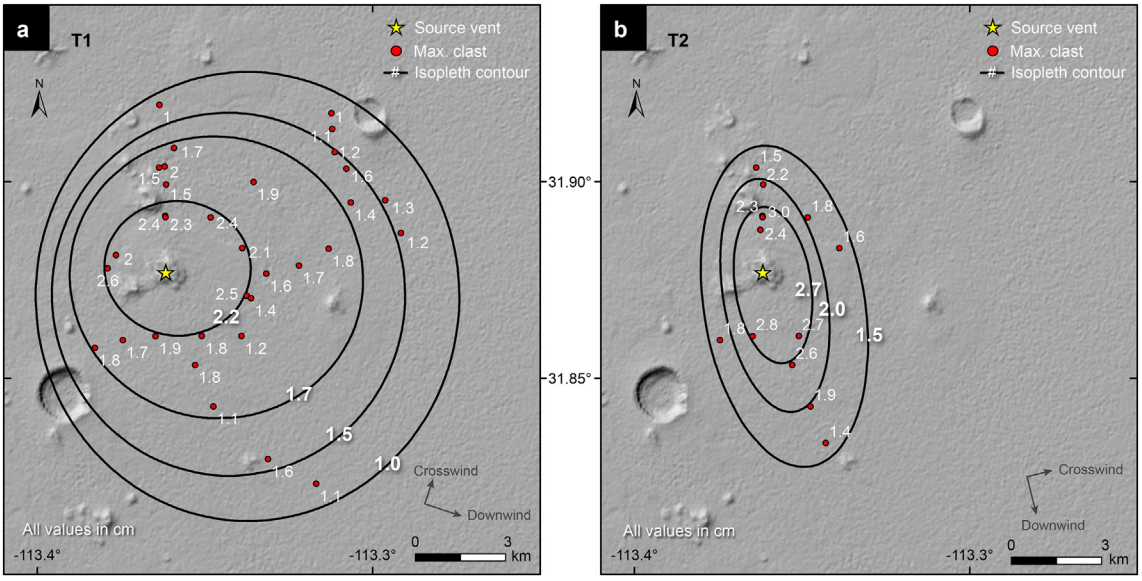

Fig. 7. Isopleth maps in centimeters for (a) T1 and (b) T2. Crosswind and downwind axes are noted.

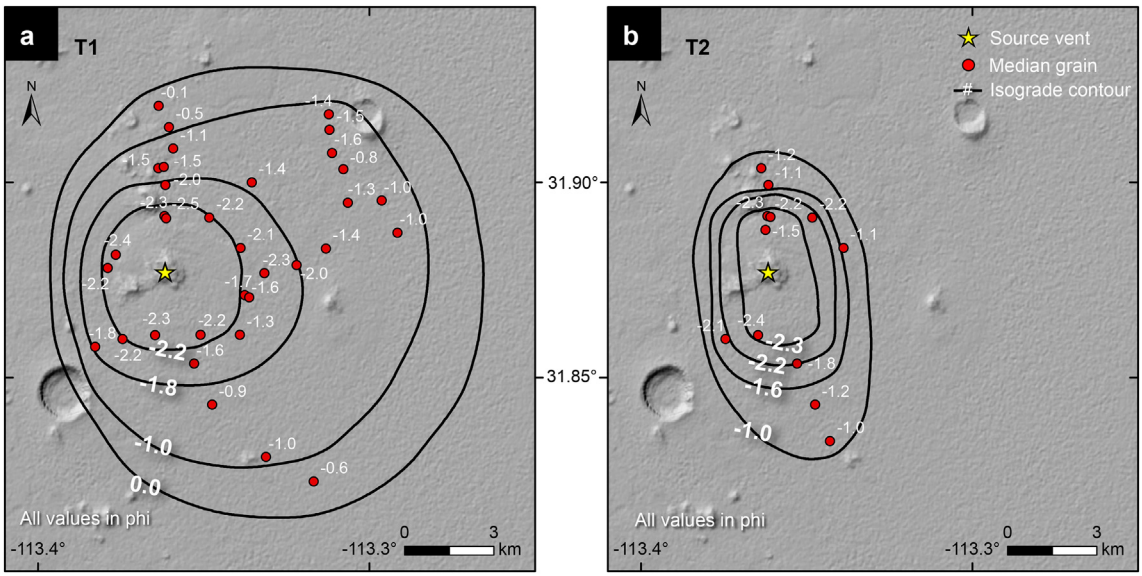

Fig. 8. Isograde maps of median grain size in phi for (a) T1 and (b) T2.

more reliable when the power-law exponent is >2 because it is less sensitive to the distal integration limits. The volumes determined by the Weibull and exponential best-fits may then be a more conservative representation of T1. However, it is important to note that given the presence of only one exponential segment, the resulting volume has to be considered a minimum (e.g., Bonadonna and Phillips, 2003; Bonadonna and Houghton, 2005).

Given the potential over-estimation from power-law best-fit and underestimation from Weibull and exponential best-fits, we take the average of all three methods as a reasonable estimate for the volume of T1 ($4.9 \pm 1.4 \times 10^7$ m^3; DRE $1.4 \pm 0.4 \times 10^7$ m^3). As discussed in Section 3.1, the upper portions of the deposit show evidence of dust infiltration, and we have excluded that layer in thickness and volume calculations. Based on the observed relative thickness of that layer over the extent of the tephra blanket, our volumes for T1 could be underestimated by ~15%. Keep in mind, however, that this 15% uncertainty accounts only for the dust infiltration in the deposit and not the erosion/burial of T1 at the distal edges of the deposit where no field measurements were possible. The distal integration limits of the power-law fitting have been selected based on a distal deposit thickness of 1 cm (Fig. 6; Fig. 18), which implies that volume calculation with this method does not account for any portion of the deposit with thickness <1 cm.

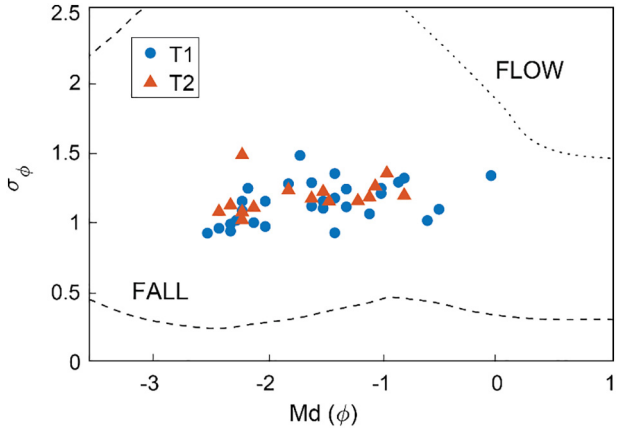

Fig. 9. Median phi grain size (ϕ) and sample standard deviation (σ_ϕ) for T1 and T2. T1 and T2 samples plot over similar ranges, but T1 shows wider degree of variability (see also Fig. 5). Pyroclastic fall and flow fields are defined following Walker (1971). $\phi = -\log_2(d)$, where d is the particle diameter in mm.

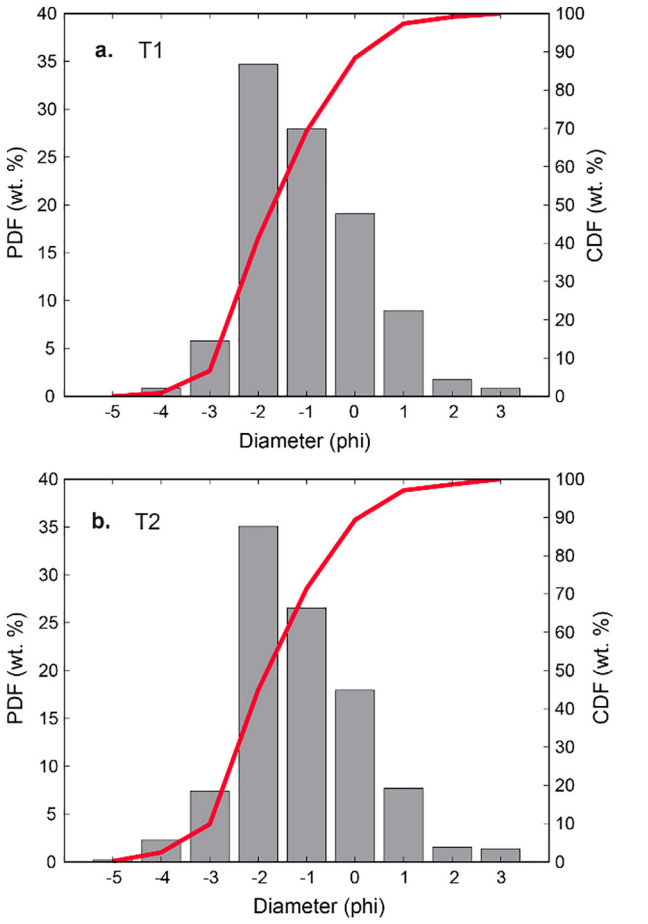

Fig. 10. Total grain size distribution for (a) T1 and (b) T2. Probability distribution function (weight percent) histogram and cumulative distribution function (weight percent) are plotted and were calculated with the Biass and Bonadonna (2014) script.

Table 1
Graphical statistical parameters for TGSD of T1 and T2. Md_ϕ is median diameter in phi, σ_ϕ is graphic standard deviation, mean (ϕ) is graphic mean, Sk is graphic skewness, and Kt is graphic kurtosis following Inman (1952). $\phi = -log_2(d)$, where d is the particle diameter in mm.

	T1	T2
Md_ϕ (ϕ)	−1.70	−1.80
σ_ϕ	1.37	1.25
Mean (ϕ)	−1.39	−1.55
Sk	0.23	0.20
Kt	0.95	1.02

The three calculation methods show much closer agreement for the volume of T2. The Weibull best-fit for T2 yielded a volume of 4.0×10^7 m^3 (DRE $1.3 \pm 0.2 \times 10^7$ m^3). An exponential best-fit for T2 yielded a volume of 3.2×10^7 m^3 (DRE $1.1 \pm 0.1 \times 10^7$ m^3), and a power-law best-fit yielded a volume of $3.8 \pm 0.2 \times 10^7$ m^3 (DRE $1.2 \pm 0.2 \times 10^7$ m^3) (Fig. 18b) (Table 4). The power-law exponent for the T2 data is >2 (Table 3), suggesting that the resulting volume is less sensitive to the choice of the distal integration limit, as also shown by the consistency of our results (Bonadonna and Houghton, 2005). Although the upper portions of T2 are impacted by dust infiltration, its areal extent is more concentrated and it does not extend into the playa region to the east. T2 thus appears to have been affected less by erosion and/or reworking than T1. Therefore, the better overall preservation and rapid thinning of T2 likely explains the closer agreement among the three methods for volume estimation (avg. $3.7 \pm 0.4 \times 10^7$ m^3; $1.2 \pm 0.2 \times 10^7$ km^3 DRE). However, based on our measurements of the dust-infiltrated layer, ignoring it could account for a ~20% underestimation in the T2 volume calculation.

Although the volumes estimated for T1 and T2 are roughly the same, the larger uncertainty associated with the calculation of the T1 volume, different depositional pattern (Fig. 6), and poorer exposure all suggest that T1 is larger in volume than what is estimated here. For each of the three calculation methods, T1 yields slightly larger volumes than T2 (Table 4). The exponential best-fit results in the lowest calculated volume for both deposits. Combining the average volumes of T1 and T2 yields a total DRE tephra volume of $2.6 \pm 0.5 \times 10^7$ m^3.

5.2. Edifice and lava volume estimates

In addition to calculating the volume of the tephra deposit, we also calculated the volumes of the Tecolote lava flows and cone (Table 5). The area of each lava flow was measured through mapping in ArcGIS, and an average thickness was determined by examining various cross sections through a 30 m/pixel regional DEM. The area was multiplied by average thickness for simplified volume calculations. Given the breached nature of the Tecolote edifice, we approximated the original shape of the Tecolote cone. We assumed the rafted wall portions found on the Q flow originally constituted the northwestern edifice wall and was a similar height to the other walls. This calculated volume will be a maximum value and we recognize the possibility that the cone may have been smaller due to the breached wall never having been entirely closed. We used the high-resolution 8 cm/pixel DEM of the Tecolote edifice from Scott et al. (2018) to determine cone dimensions and volume (Fig. 12). The Tecolote cone has a diameter of ~1.1 km, and its walls are ~155 m tall. The interior crater is ~400 m across and ~80 m deep. We estimated a bulk density of 1500 kg/m^3 for the cone and 2200 kg/m^3 for the lava flows. To convert to DRE volumes, we assumed a DRE value for an alkali basalt to be 2700 kg/m^3.

The Q flow and S flow constitute the majority of the total Tecolote volume, with DRE volumes of 0.083 km^3 and 0.082 km^3 respectively (Table 5). The smaller lava flows A, B, C, R, and T have volumes orders of magnitude smaller and combine to have a DRE volume of only 1.47×10^{-3} km^3. The cone itself has a smaller volume than either of the two large lava flows with a DRE volume of 0.041 km^3. The two tephra units combined (0.026 ± 0.005 km^3 DRE) are approximately half that of the cone. The total erupted products have a DRE volume of 0.23 km^3 (Table 5, Fig. 19). Erupted volumes from other Pinacate vents range from 0.001–1 km^3 (Lynch, 1981).

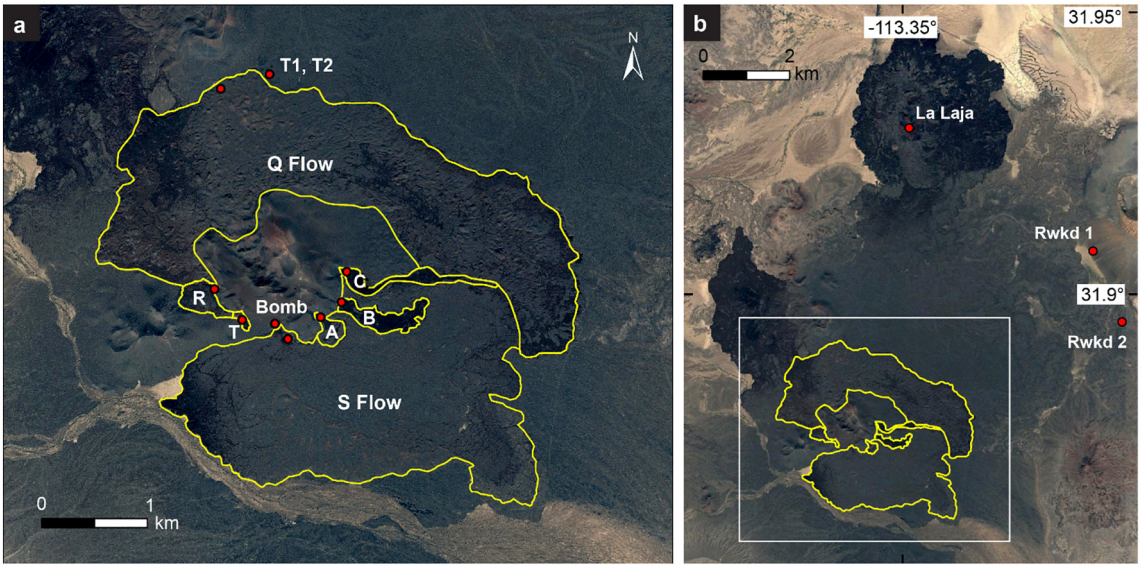

Fig. 11. Map of Tecolote's seven lava flows with location of samples for geochemical analyses. (a) Tecolote's seven mapped lava flows (A, B, C, Q, R, S, T). Geochemical samples are indicated by red dots and were collected from all lava flows, a bomb, and T1 and T2 tephra. (b) Location of scoria sample collected from the La Laja cone and two reworked tephra samples (Rwkd #) indicated by red dots. Tecolote inset (Panel a) outlined in white. (For interpretation of the references to color in this figure legend, the reader is referred to the web version of this article.) *Images from Google Earth.*

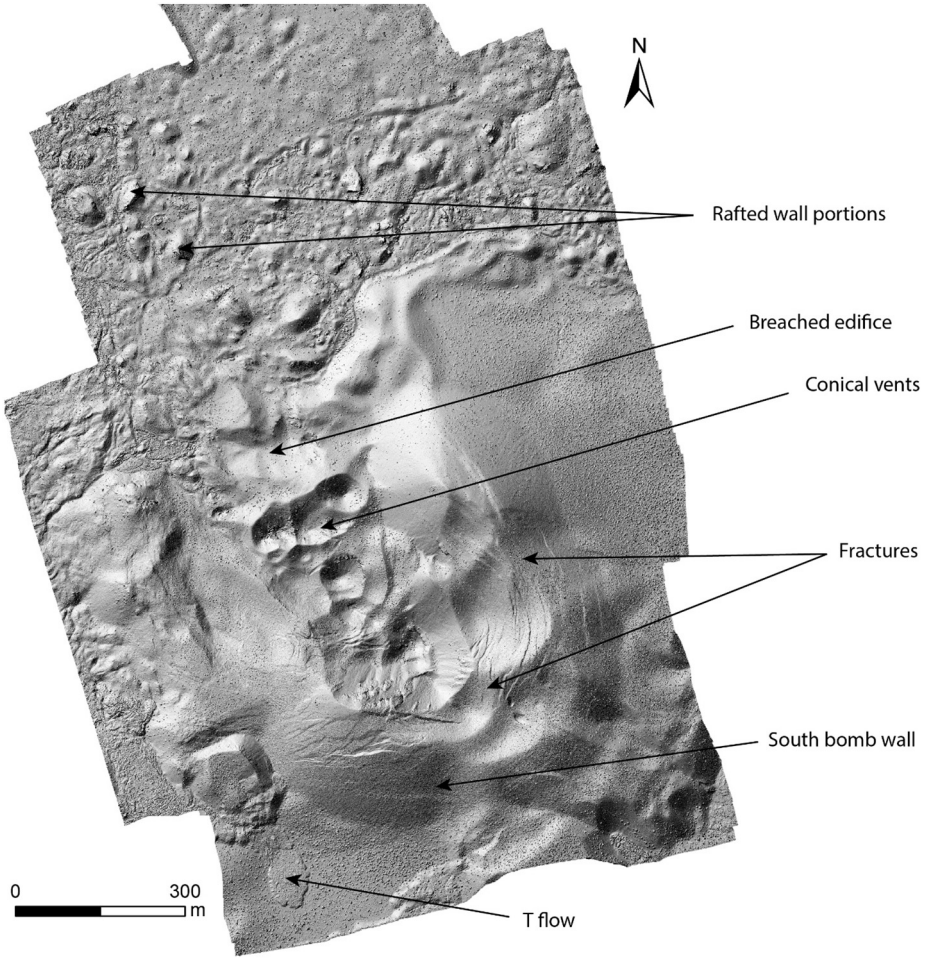

Fig. 12. Topographic model of the Tecolote edifice and adjacent lava flows with annotated features. Model was produced from 2024 sUAS-derived aerial photographs using the Structure-from-Motion (SfM) method. Hillshade of 8 cm/pixel digital elevation model illuminated from the northwest. Scott et al. (2018).

5.3. Column height and mass eruption rates

We used two methods to calculate plume heights for the T1 and T2 eruptive episodes. We first employed the Biass et al. (2015) implementation of the model from Carey and Sparks (1986), which constrains plume height and wind speed from the maximum downwind and cross-wind range of an isopleth contour (Fig. 7). We use scoria clasts due to a lack of lithics in our deposit. We did not observe broken scoria or evident fracture faces on the clasts used. Given the use of scoria clasts over lithics, we therefore consider the associated estimation of plume height relatively conservative. To determine clast density, we measured the density of the 5 largest clasts from each unit in two pits. The T1 clast density is ~1500 ± 250 kg/m^3 whereas the T2 clast density is ~1700 ± 370 kg/m^3. Given the low height of the cone above the sampling locations (<200 m), we assume the calculated column height to be the height above the vent.

We also calculated column heights following Rossi et al. (2019), which refines and updates the method for column height reconstruction introduced by Carey and Sparks (1986). In particular, Rossi et al. (2019) make adjustments to account for wind advection of the rising plume.

Reconstructed column heights for the T1-producing episode ranged between 12.4 and 19.8 km, with wind speeds between 3 and 7 m/s (Table 6) following Carey and Sparks (1986). The 1.75, 1.5 and 1.0 cm contours yielded relatively consistent column heights for an average column height of ~18 km. However, the 2.2 cm contour for T1 yielded a substantially lower column height and lower wind speed than the other contours. This lower column height may be due to the fact that deposition along this contour occurred from the base of the vertical plume and not from the upper umbrella region of the plume. Thus, we choose a column height of ~18 km and wind speed of 7 m/s as reasonable estimates for the T1 plume based on this model.

Using the Rossi et al. (2019) model, we assign an intermediate eruption intensity for T1, which is recommended for events with an initial plume radius of 50–200 m, spanning the range typical for most steady, explosive volcanic eruptions. The intermediate intensity model yields a column height of ~15 km for T1 (Table 6). This column height is lower than the ~18 km column height calculated with the Carey and Sparks (1986) model as it accounts for the effect of wind on plume rise even though the plume was not strongly bent over. Rossi et al. (2019) find that their computed column heights are generally 5–23% lower than those computed with the Carey and Sparks (1986) model. The Rossi et al. (2019) model also yields a lower wind speed for T1, ≤1 m/s.

T2's isopleth contours yield column heights ranging from 9.8 to 13.2 km and wind speeds between 14 and 17 m/s (Table 7) following the Carey and Sparks (1986) model, with averages of ~11 km and ~15 m/s. The column heights are smaller than those estimated for T1, consistent with waning explosivity during the latest stages of the eruption. The reconstructed wind speeds are nearly double that for T1, indicating a shift in meteorological conditions between the two explosive episodes.

Fig. 13. Portion of rafted edifice wall on Q flow, ~1 km directly north of central Tecolote vent.

Using nomograms from Rossi et al. (2019) for an eruption of low intensity, which is recommended for weak or bent plumes, a column height of ~12 km is reconstructed for T2 (Table 7) and is reasonably consistent with the ~11 km column height from the Carey and Sparks (1986) model. However, the Rossi et al. (2019) model reconstructs a lower wind speed for T2, on the order of ~7 m/s. It is important to note that the strategies of both Carey and Sparks (1986) and Rossi et al. (2019) are of difficult application to T2 given the double elongation of the associated isopleth map that indicates wind-shear and/or fissural character of the eruption, aspects that are not described by the two models.

From a given plume height, we also derived a corresponding mass eruption rate (MER) following Wilson and Walker, (1987), Mastin et al. (2009), and Degruyter and Bonadonna (2012). A column height of 18 km for T1 from the Carey and Sparks (1986) model corresponds to an average MER of $2.2 \pm 1.2 \times 10^7$ kg/s. The lower column height of 15 km for T1 from the Rossi et al. (2019) model corresponds to an average MER of $1.0 \pm 0.6 \times 10^7$ kg/s. For a T2 column height of 11 km, the average MER is $3.2 \pm 1.4 \times 10^6$ kg/s, an order of magnitude lower than that of T1. All modeled column heights and MERs are summarized in Table 6 (T1) and Table 7 (T2).

Using the calculated volumes (Table 5) and the deposit densities, along with the estimated MERs (Tables 6 & 7), we approximate the eruption duration of both tephra-producing episodes (Table 8). Using this technique, we estimate the duration of the T1 episode to be between approximately 40 ± 25 min to 80 ± 50 min, while the T2 episode was longer, likely lasting approximately 3 ± 1 h. If we consider only the MER following Degruyter and Bonadonna (2012), T1 would have a longer duration of approximately 105 ± 50 min and T2 a duration of approximately 4.5 h. Because the volumes used here are likely to be minimum values, these durations are also thought to be minima.

5.4. Eruption classification

To classify the two tephra-producing eruptions, we followed the classification schemes of both Pyle (1989) and Bonadonna and Costa (2013). The Pyle scheme uses parameters b_t, the thickness half-distance, and b_c, the clast half-distance.

For T1, b_t is 1.70 km and b_c is 3.19 km. For T2, b_t is 0.46 km and b_c is 1.66 km. The T1 data plot just within the Plinian range near the boundary with subplinian, and the T2 data plots within the subplinian range. As a comparison, the b_t values determined for basaltic Plinian eruptions are all above 2 km: 4.3 km for Tarawera 1886 (Sable et al., 2006), 2.7 km for Etna 122 BCE (Coltelli et al., 1998), and 2, 5, and 6 km for unit B, C, and D + E + F of Fontana Lapilli (Constantini et al., 2009). The b_t value of T1 is therefore consistent with a subplinian style similar to Cerro Negro 1992 (b_t = 1.4 km; Connor and Connor, 2006). Unit 2 of Sunset Crater is characterized as a Strombolian to violent Strombolian phase, but its b_t value of 1.9 km is significantly higher than the b_t value for T2 (Alfano et al., 2018). The violent Strombolian phases of Parícutin and El Jorullo have been characterized with the Walker (1973) scheme rather than Pyle (1989) and do not have published b_t values for comparison (Pioli et al., 2008; Rowland et al., 2009).

The b_t values are well constrained due to the high number of isopach contours available, whereas the b_c values are defined by only 3–4 isopleth contour points. While the ~3 km b_c value calculated for T1 suggests a column height of 29 km, the Carey and Sparks (1986) model suggests a substantially lower column height of ~18 km and the Rossi et al. (2019) model an even lower column height of ~15 km. The mismatch between column heights and eruption classification following Pyle (1989) likely stems from a poor constraint on b_c and the effect of wind on the plume and tephra dispersal, which is not accounted for in the classification of Pyle (1989).

We also follow two classification schemes from Bonadonna and Costa (2013). The first method categorizes eruptions based on column height vs. mass eruption rate. The T1 column height of ~18 km from the Carey and Sparks (1986) model and averaged MER of $2.2 \pm 1.2 \times 10^7$ kg/s plots squarely within the subplinian range. The column height of ~15 km from the Rossi et al. (2019) model and corresponding MER of $1.0 \pm 0.6 \times 10^7$ kg/s for T1 still plots within the subplinian range, but toward the lower end of the classification. The T2 column height of ~11 km and averaged MER of $3.2 \pm 1.4 \times 10^6$ kg/s plots in the small–moderate range.

The second method we follow from Bonadonna and Costa (2013) uses Weibull fits to thickness and median grain size data from isopach (Fig. 6) and isograde maps (Fig. 8) to define the parameters λ_{th} and $\lambda_{Md\phi}$. For T1, we solved for a λ_{th} of 10.8 km and a $\lambda_{Md\phi}$ of 10.5 km. For T2, we solved for a λ_{th} of 3.1 km and a $\lambda_{Md\phi}$ of 6.6 km. The T1 data plot near the upper 20% error bars of subplinian, and T2 plots near the 20% error bar intersection of subplinian and small-moderate. These classifications are consistent with the first classification scheme from Bonadonna and Costa (2013) and overall suggest that T1 was produced by a subplinian eruption, and T2 was produced by a small-moderate eruption, likely violent Strombolian given the estimated column height (Walker, 1973; Valentine et al., 2006; Pioli et al., 2008).

6. Discussion

6.1. Tectonic setting

The geochemistry of the deposits presented here supports previous research that finds no obvious influence from Gulf of California opening

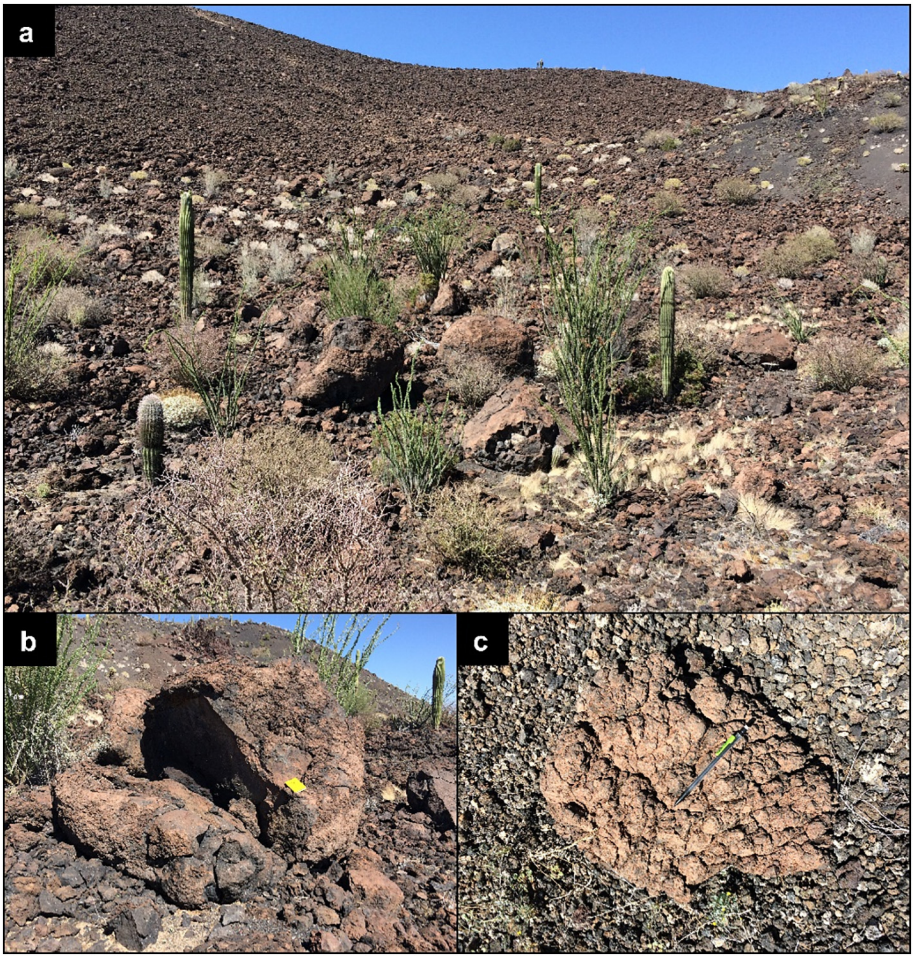

Fig. 14. (a) Southern exterior wall of Tecolote edifice, which is littered with bombs of various sizes. (b) Large ~2 m diameter bomb, sampled for geochemistry. (Notebook for scale.) (c) Cauliflower-type bomb.

on Pinacate volcanism (Lynch et al., 1993). Volcanism appears more similar to intraplate volcanism like that observed in the San Francisco volcanic field, Arizona (Alibert et al., 1986) and other Quaternary monogenetic volcanic fields of the Basin and Range province (Valentine et al., 2017). By comparison with other Quaternary volcanic provinces near the Gulf of California, the San Quintín volcanic field in northern Baja California along the western coast of the Baja peninsula is the only volcanic field in Baja that has been found to have OIB signatures (Storey et al., 1989; Luhr et al., 1995). The San Quintín lavas are unique for their OIB signatures in Baja, as the predominant lava types at other volcanic fields

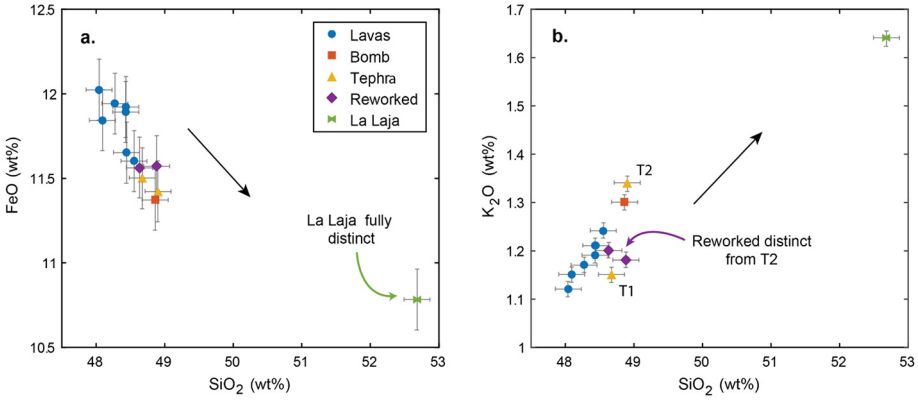

Fig. 15. Abundances of (a) FeO and (b) K_2O vs. SiO_2 for the Tecolote lavas, bomb, and tephra; reworked tephra; and La Laja scoria sample. Arrows indicate general trend through sequence.

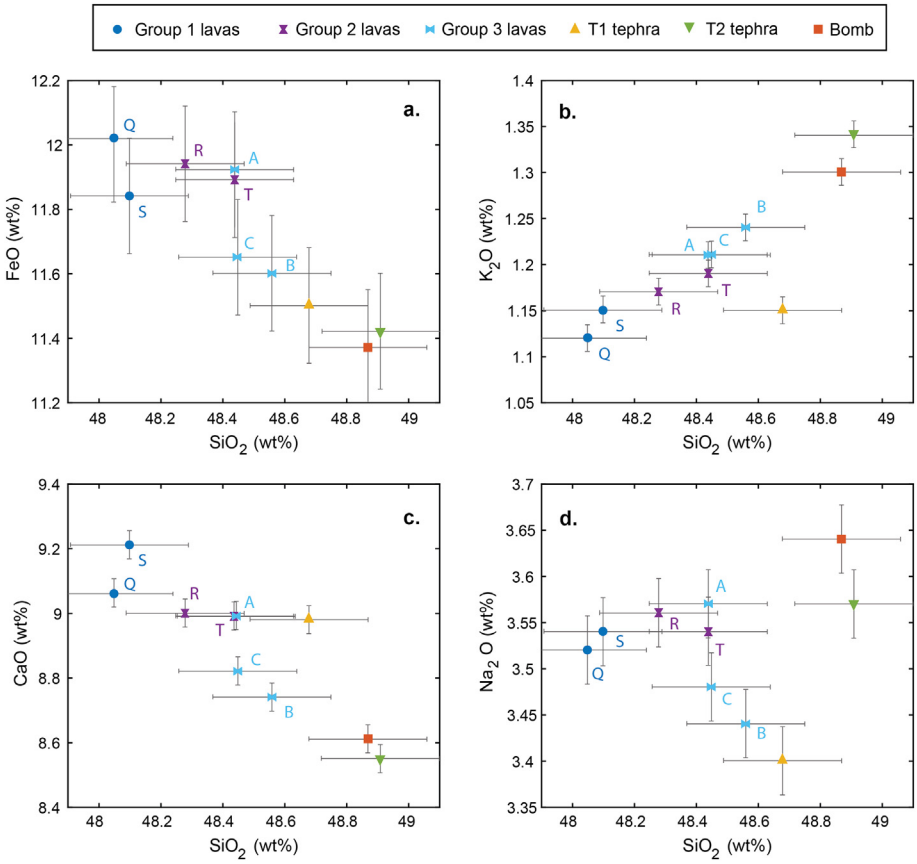

Fig. 16. Abundances of (a) FeO, (b) K_2O, (c) CaO, and (d) Na_2O vs. SiO_2 for the Tecolote lavas, tephra, and bomb samples. Q and S are Group 1 lavas, R and T are Group 2 lavas, and A, B, and C are Group 3 lavas.

(e.g. Jaraguay, San Borja) are magnesian basaltic andesites locally known as 'bajaites,' which are related to the cessation of ridge subduction and transition to rifting (Rogers et al., 1985). The northwest coast of mainland Sonora is absent of Quaternary volcanic fields comparable to the Pinacate.

Within a broader regional context, Rio Grande Rift basalts <10 Ma and Basin and Range basalts <5 Ma also have been found to have signatures similar to that of OIBs (Fritton et al., 1991; McMillan et al., 2000). Multiple factors support a connection of Pinacate volcanism with Basin and Range mantle dynamics rather than Gulf of California opening (Gutmann, 2007): (1) OIB-like magmas appeared around ~5 Ma in the Basin and Range province, (2) Pinacate volcanism began ~2 Ma and its rocks match an OIB trend, and (3) alignment of Pinacate vents overall exhibit a structural control reflective of the current Basin and Range stress regime (Lutz and Gutmann, 1995). OIB-type signatures have been found at other intraplate volcanic fields in close spatial distance to plate boundaries, such as the Mexican volcanic belt (Márquez et al., 1999; Petrone et al., 2003), indicating that immediate tectonic setting may not always have a dominant control on magma petrogenesis.

Table 2
Major element geochemical analyses from the Tecolote lavas (A, B, C, Q, R, S, T), bomb, tephra (T1 and T2), reworked tephra (Rwkd#), and La Laja scoria. All values are normalized element weight percent. Analysis precision is 2σ and is listed in the final column.

	Flow A	Flow B	Flow C	Flow Q	Flow R	Flow S	Flow T	Bomb	T1 tephra	T2 tephra	La Laja	Rwkd1	Rwkd2	2 σ
SiO_2	48.44	48.56	48.45	48.05	48.28	48.10	48.44	48.87	48.68	48.91	52.69	48.64	48.89	0.19
TiO_2	2.477	2.383	2.411	2.482	2.498	2.465	2.478	2.347	2.457	2.326	1.812	2.36	2.34	0.012
Al_2O_3	16.24	16.24	16.07	16.06	16.14	16.18	16.28	16.04	16.36	16.31	15.41	16.18	16.24	0.082
FeO[a]	11.92	11.60	11.65	12.02	11.94	11.84	11.89	11.37	11.50	11.42	10.78	11.56	11.57	0.18
MnO	0.181	0.178	0.177	0.178	0.180	0.177	0.182	0.177	0.178	0.172	0.166	0.17	0.17	0.002
MgO	6.51	7.19	7.31	7.07	6.78	6.88	6.55	7.22	6.85	6.97	6.34	7.19	7.18	0.073
CaO	8.99	8.74	8.82	9.06	9.00	9.21	8.99	8.61	8.98	8.55	6.89	8.94	8.82	0.043
Na_2O	3.57	3.44	3.48	3.52	3.56	3.54	3.54	3.64	3.40	3.57	3.86	3.34	3.20	0.036
K_2O	1.21	1.24	1.21	1.12	1.17	1.15	1.19	1.30	1.15	1.34	1.64	1.20	1.18	0.015
P_2O_5	0.463	0.430	0.429	0.439	0.450	0.445	0.464	0.417	0.437	0.434	0.411	0.41	0.41	0.003

[a] Major elements are normalized on a volatile-free basis, with total Fe expressed as FeO.

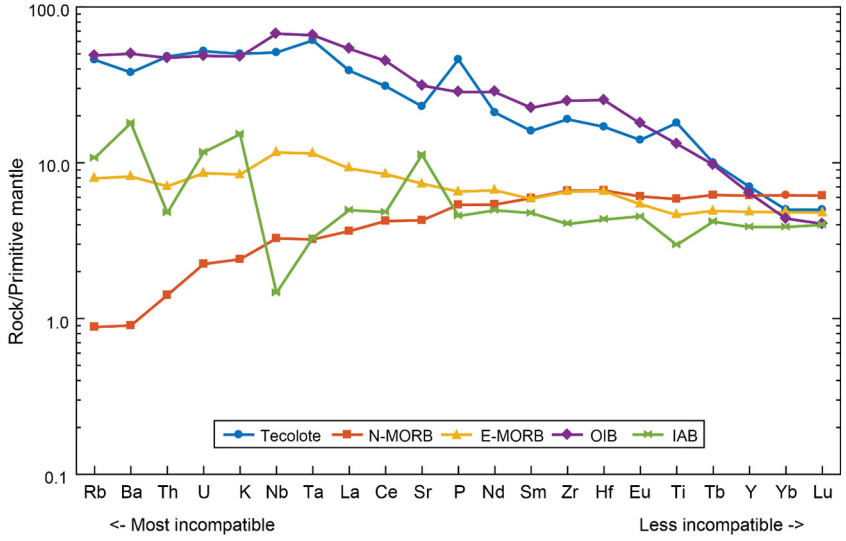

Fig. 17. Primitive mantle-normalized spider diagram of incompatible elements from all analyzed Tecolote samples compared to trends of normal-type mid-ocean ridge basalt (N-MORB), plume-type mid-ocean ridge basalt (E-MORB), ocean island basalt (OIB), and island arc basalt (IAB). Values for primitive mantle, N-MORB, E-MORB, and OIB are from Sun and McDonough (1989). Values for IAB are from Ewart et al. (1998).

Fig. 18. Plots of thickness vs. area$^{1/2}$ for volume calculations with Weibull, exponential, and power-law best-fits for (a) T1 and (b) T2. See Table 3 for equation line fits.

6.2. Eruptive parameters and classification

Tecolote's erupted volume (DRE) is dominated by lava flows, which constitute approximately 71% of the erupted volume. This effusive volume is dominated by the first two lava flows that opened the eruption. The remainder of the production consists of scoria, with roughly 18% of the total eruption volume in the cone, and about 11% in the tephra blanket. Alfano et al. (2018) compiled total erupted volumes from various basaltic eruptions and found that the average tephra/cone ratio was 0.7 ± 0.3. For the Tecolote sequence, the tephra/cone ratio is ~0.6, which is in good agreement with the observed trend. In terms of total volume, the Tecolote eruption is similar to the Cerro Negro eruption of 1850–1995 (Hill et al., 1998) and Tolbachik Cone 1 (1975; Budnikov et al., 1983). The distribution between lava, cone, and tephra is similar to the Tolbachik Cone 2 eruption (1975; Budnikov et al., 1983), which was approximately 1.6 times larger in volume than the Tecolote eruption.

Table 3
Weibull, exponential, and power-law best-fit equations for T1 and T2 (Fig. 18).

	T1
Weibull	$T = 23.802(x/10.755)^{-0.725}\exp[-(x/10.755)^{1.275}]$
Exponential	$T = 81.904\exp^{-0.205x}$
Power-law	$T = 299.11x^{-1.495}$
	T2
Weibull	$T = 233.754(x/3.144)^{-0.846}\exp[-(x/3.144)^{1.154}]$
Exponential	$T = 569.70\exp^{-0.595x}$
Power-law	$T = 1187x^{-2.344}$

Table 4
Calculated volumes for the T1 and T2 tephra based on Weibull best-fit, exponential best-fit, and power-law best-fits. Volumes are listed both as bulk and dense rock equivalent (DRE).

	T1 ($\times10^7$ m^3)	T1 DRE ($\times10^7$ m^3)	T2 ($\times10^7$ m^3)	T2 DRE ($\times10^7$ m^3)	Total tephra DRE ($\times10^7$ m^3)
Weibull	4.3	1.2 ± 0.1	4.0	1.3 ± 0.2	2.5 ± 0.2
Exponential	3.9	1.1 ± 0.1	3.2	1.1 ± 0.1	2.2 ± 0.1
Power-law	6.4 ± 0.5	1.8 ± 0.2	3.8 ± 0.2	1.2 ± 0.2	3.1 ± 0.3
Average	4.9 ± 1.4	1.4 ± 0.4	3.7 ± 0.4	1.2 ± 0.2	2.6 ± 0.5

Table 5
Calculated volumes of the Tecolote, lava flows, cone, and tephra units.

Flow	Area (km^2)	Avg. thickness (m)	Volume (m^3)	Volume (m^3 DRE)	Volume (km^3 DRE)
Q flow	5.35	19	1.0×10^8	8.3×10^7	0.083
S flow	5.02	20	1.0×10^8	8.2×10^7	0.082
R flow	0.104	5.5	5.7×10^5	4.7×10^5	4.68×10^{-4}
T flow	1.45×10^{-2}	4	5.8×10^4	4.7×10^4	4.71×10^{-5}
A flow	5.51×10^{-2}	3	1.6×10^5	1.3×10^5	1.34×10^{-4}
B flow	0.144	4	5.8×10^5	4.7×10^5	4.69×10^{-4}
C flow	0.125	3.5	4.4×10^5	3.6×10^5	3.56×10^{-4}
All flows	–	–	2.1×10^8	1.7×10^8	0.166
Cone	–	–	7.3×10^7	4.1×10^7	0.041
T1 tephra	–	–	$4.9 \pm 0.1 \times 10^7$	$1.4 \pm 0.4 \times 10^7$	0.014±0.004
T2 tephra	–	–	$3.7 \pm 0.4 \times 10^7$	$1.2 \pm 0.2 \times 10^7$	0.012±0.002
Total	–	–	5.8×10^8	2.3×10^8	0.233

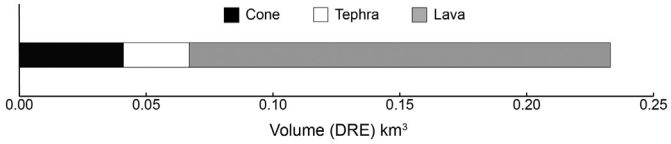

Fig. 19. Distribution of cone, tephra, and lava DRE volume.

The total DRE volume of the erupted products from Tecolote is approximately half that of Sunset Crater (0.52 km^3), which is the most explosive monogenetic eruption studied to date (Alfano et al., 2018). Approximately 50% of Sunset Crater's total DRE erupted volume was tephra, while the two tephra units from Tecolote constitute approximately only 11% of the total volume produced. Despite the fact that effusive products dominated Tecolote's total volumetric production, the most explosive phase (T1) is of similar magnitude to the

Table 6
Parameters used for T1 column height calculation, along with calculated column height (Carey and Sparks, 1986; Biass et al., 2015; Rossi et al., 2019), wind speed, and MER.

Model	Clast size (cm)	Downwind distance (km)	Crosswind distance (km)	Column height (km)	Wind speed (m/s)	MER_{ww}[a] (kg/s)	MER_m[b] (kg/s)	MER_{db}[c] (kg/s)
Carey and Sparks (1986)	2.2	2.8	2.4	12.4	3	7.6×10^6	4.8×10^6	2.5×10^6
	1.7	6.6	17.2	17.2	6	2.8×10^7	1.9×10^7	1.1×10^7
	1.5	8.0	18.3	18.3	7	3.6×10^7	2.4×10^7	1.5×10^7
	1.0	9.8	19.8	19.8	7	4.9×10^7	3.4×10^7	2.1×10^7
Rossi et al. (2019)	2.2	2.8	2.4	13.9	1	1.2×10^7	7.7×10^6	3.2×10^6
	1.7	6.6	17.2	14.9	–	1.6×10^7	1.0×10^7	4.3×10^6
	1.5	8.0	18.3	15.0	–	1.6×10^7	1.1×10^7	4.4×10^6
	1.0	9.8	19.8	15.0	–	1.6×10^7	1.1×10^7	4.5×10^6

[a] Calculated with Wilson and Walker, (1987) formula.
[b] Calculated with Mastin et al. (2009) relation.
[c] Calculated with Degruyter and Bonadonna (2012) expression.

Table 7
Parameters used for T2 column height calculation, along with calculated column height (Carey and Sparks, 1986; Biass et al., 2015; Rossi et al., 2019), wind speed, and MER.

Model	Clast size (cm)	Downwind distance (km)	Crosswind distance (km)	Column height (km)	Wind speed (m/s)	MER_{ww}[a] (kg/s)	MER_m[b] (kg/s)	MER_{db}[c] (kg/s)
Carey and Sparks (1986)	2.7	3.1	1.4	9.8	14	3.0×10^6	1.8×10^6	1.8×10^6
	2.0	4.8	1.9	10.7	17	4.2×10^6	2.6×10^6	2.9×10^6
	1.5	6.7	3.0	13.2	15	9.8×10^6	6.3×10^6	6.2×10^6
Rossi et al. (2019)	2.7	3.1	1.4	12.3	7	7.3×10^6	4.6×10^6	3.2×10^6
	2.0	4.8	1.9	12.2	–	7.1×10^6	4.5×10^6	3.0×10^6
	1.5	6.7	3.0	13.0	–	9.1×10^6	5.8×10^6	3.9×10^6

[a] Calculated with Wilson and Walker, (1987) formula.
[b] Calculated with Mastin et al. (2009) relation.
[c] Calculated with Degruyter and Bonadonna (2012) expression.

Table 8
Calculated eruption durations based on the different MER calculations.

Phase	Column height (km)	MER_{ww}[a] (kg/s)	MER_m[b] (kg/s)	MER_{db}[c] (kg/s)	$Duration_{ww}$[a] (min)	$Duration_m$[b] (min)	$Duration_{db}$[c] (min)	Avg. duration (min)
T1	18	3.4×10^7	2.7×10^7	1.1×10^7	18	27	67	38 ± 26
T1	15	1.6×10^7	1.1×10^7	5.3×10^6	38	58	140	79 ± 54
T2	11	4.7×10^6	2.9×10^6	2.4×10^6	117	188	273	193 ± 78

[a] Calculated with Wilson and Walker, (1987) MER formula.
[b] Calculated with Mastin et al. (2009) MER relation.
[c] Calculated with Degruyter and Bonadonna (2012) MER expression.

subplinian explosive phases reported from Sunset Crater (Alfano et al., 2018). Both of Tecolote's explosive phases were of greater magnitude than the primarily Strombolian and violent Strombolian phases of Parícutin, although Parícutin produced a total erupted volume approximately 5 times larger than Tecolote during its nearly decade-long eruption (Pioli et al., 2008).

We emphasize here that very few highly-explosive basaltic eruptions have been classified using the existing schemes presented here, and the evident inconsistences among methods highlight the need for further investigation to design appropriate field-based classification methodologies for such events. Two of the eruption classification schemes we used from Bonadonna and Costa (2013) were consistent with one another. The first scheme using column height vs. mass eruption rate is simple to employ, but it is dependent on the model used to determine column height and MER. While our variances in column height calculation method did not change the classification for T1, this scheme is only secondarily tied to measurable deposit characteristics. The second scheme from Bonadonna and Costa (2013) using a Weibull fit for thinning and median grain size trends is likely the most robust classification approach for our deposit. It directly relies on measurable physical characteristics from the deposit, rather than model-derived results. However, this scheme uses isograde of median grain size, which are not often published or readily obtained.

Despite the variations in classification, there is strong evidence that T1 was a significant subplinian eruption. The event was short-lived, but the column height was probably between 15 to 18 km. T2 may have been a less violent eruption, classified as violent Strombolian, producing a ~11-km-high plume, but it appears to have had a significantly longer duration than T1, although some of the detailed stratigraphic characteristics of T2 suggest that the activity could have been pulsatory with variable eruption rates. Further work will probe within-unit variations in order to further document unsteadiness in eruption rate and/or wind velocity and begin to understand the role plumbing system characteristics played in effusive and significant explosive phases.

6.3. Chronology and dynamics

The Tecolote eruption generally follows the pattern of Pinacate field volcanic activity (Gutmann, 1979), although it appears to have had a final stage of low-volume effusive volcanism after the last bursts of tephra emplacement and more significant tephra-producing phases. Additionally, the eruption complicates the division into four distinct stages as described by Gutmann (1979), as multiple stages appear to have been simultaneous. The general proposed chronology of the eruption is depicted in Fig. 20.

The Q flow and S flow constitute the basal lava flows. Q flow eruption must have been contemporaneous with cone building, as large rafted portions of the edifice wall material are found on the Q flow up to 3.6 km from the vent. Although there is no evidence for impoundment of a lava lake prior to breaching, the cone was likely breached as vent activity migrated northwestward and caused the northwest wall

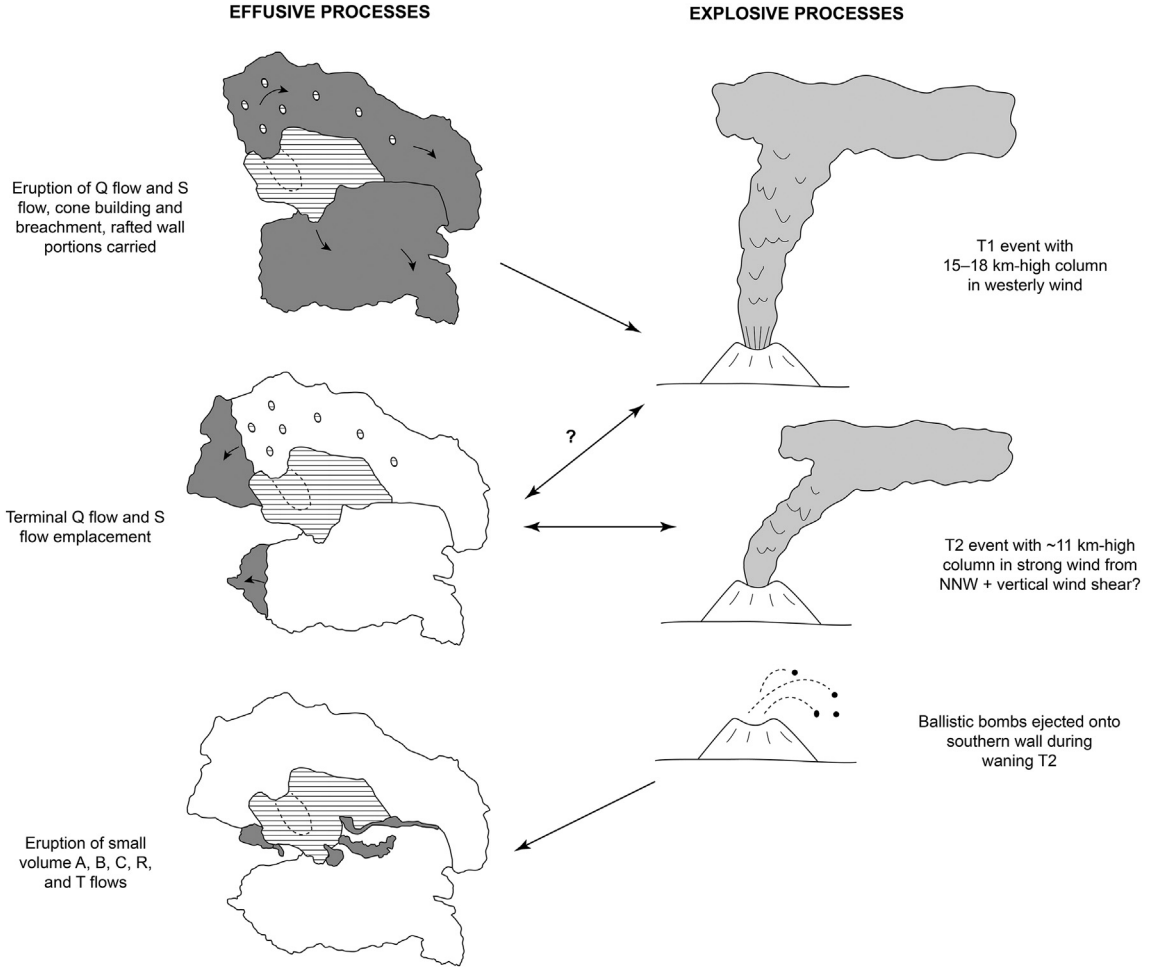

Fig. 20. Generalized chronology of the Tecolote eruption divided into effusive and explosive processes. The eruption switched from effusive to explosive back to effusive behavior, with simultaneous effusive and explosive stages.

to fail (Lynch, 1981). New wall material was likely constructed and rafted away on the flow. T2, and possibly T1, must have been contemporaneous with the later stages of Q flow and S flow emplacement, as the western edges of the flows are either depleted of or devoid of tephra cover. The large bombs that mantle the exterior southern wall were likely ejected during the waning stages of T2. Unlike the majority of documented Pinacate activity, the Tecolote eruption concluded with the eruption of the small volume lava flows R, T, A, B, and C after the terminal pyroclastic eruptions. The eruption therefore exhibits at least two key shifts in eruption style between effusive and explosive behavior, as has been documented at other monogenetic centers (Valentine et al., 2006; Di Traglia et al., 2009; Pioli et al., 2008; Genareau et al., 2010; Alfano et al., 2018).

The overall eruption progression and corresponding chemical evolution suggests a complex plumbing system, possibly indicating substantial time between eruptive phases or a range of temporary storage zones at different depths that fed the different phases. The temporal evolution of the eruption shows a gradual evolution of the magma that may be explained by crystallization of calcic plagioclase, with the exception of T1 which in all plots sits off-trend (Fig. 16). T2 marks the end of the evolutionary trend, which could be consistent with the explosive nature of the eruption. The simultaneous nature of the effusive and explosive behavior suggests a single source with co-existing heterogeneous pockets of magma, where the T1 source originated from a batch of melt that was slightly more evolved and gas-rich due to crystallization (Nakagawa et al., 1999). Alternatively, gas segregation processes may have led to heterogeneous zones at a range of depths in the plumbing system (Pioli et al., 2008; Pioli et al., 2009). Ongoing investigations of melt inclusions and tephra textures aim to test these ideas and better understand the relationship between T1 and the rest of the sequence.

Regarding the two explosive phases, there seems to have been a shift in eruption and atmospheric conditions between T1 and T2. T1 appears to be associated with a strong plume (~15–18 km high) in a westerly wind (~1–7 m/s), whereas T2 appears to be associated with a weak plume (~11 km high) in a stronger wind from the NNW, possibly up to 7 m/s or up to 15 m/s, depending on the model used to derive wind speeds. A significant shift in eruption conditions for the T1 and T2 episodes could be due to magmatic differences from heterogeneous sources, changes in feeder system geometry, and/or variable ascent rates and corresponding differences in gas-escape efficiency.

While we do consider the possibility that the T2 episode was a bent-over plume, one argument against this idea is the significant upwind deposition apparent in the isopach data. One possibility is that T2 was produced by a fissure eruption with orientation that roughly matches the trend of cone breach. Although no obvious evidence of fissure activity exists to the SSE of the cone, any associated vents may have been obscured by ongoing lava flow activity.

A more likely explanation, however, is a combination of complex wind patterns and/or fluctuating column height during the T2-producing eruption. For example, the wind direction may have shifted 180 degrees from the dominant SSE direction for part of the T2 eruption. Or, there may have been vertical wind shear above the vent, such that the plume was interacting with different wind directions at different elevations or periods of the eruption. Both a temporal 180-degree shift in wind direction and vertical wind shear at approximately 4 km above the vent are supported by recent wind grams for the region derived from EDAS40 assimilation data from NOAA (NOAA-Air Resources Laboratory).

7. Conclusions

Tecolote volcano is the source vent of the tephra deposit, which is composed of two main units representing significant explosive eruptive episodes. The T1 tephra was produced by a subplinian eruption with a column height of 15–18 km and a duration of 38 ± 26 to 79 ± 54 min. The T2 tephra was produced by a violent Strombolian eruption with an approximately 11 km-high plume and substantially longer duration of 193 ± 78 min. IRSL ages are consistent with, but cannot better constrain, the age of the eruption (27 ± 6 ka, $^{40}Ar/^{39}Ar$; Gutmann et al., 2000).

Tecolote produced both lava flows and explosive phases, sometimes simultaneously, with the initial two lava flows constituting the bulk of the total erupted DRE volume. The distribution of the eruption is similar to the Tolbachick Cone 2 eruption of 1975 (Budnikov et al., 1983), and its most explosive phase was of similar magnitude to the explosive phases documented from Sunset Crater (Alfano et al., 2018). The chemistry of the different phases suggests that a slowly evolving magma batch fed most of the eruptions, aside from T1, which may have been fed by an isolated gas-rich zone of a heterogeneous magma supply. Pinacate volcanism shares geochemical signatures similar to OIBs and appears most related to intraplate volcanism of the Basin and Range province.

Acknowledgements

We thank La Reserva de la Biosfera el Pinacate y Gran Desierto de Altar for their assistance with field work permissions.

We thank Kelly Vote, Erika Groh, Sean Peters, Kyle Mohr, and Dominique Garello for their assistance with field work and Sebastien Biass for assistance in the application of the Voronoi script.

This research was funded by a Geological Society of America Graduate Student Research grant.

We thank Greg Valentine and Steve Self for their helpful comments on this manuscript.

Appendix A. Methods

Volume calculations

The Weibull method (following Bonadonna and Costa, 2012) calculates thickness T (cm) based on the relation:

$$T = \theta_{th}\left({}^{x}/_{\lambda_{th}}\right)^{n_{th}-2}\exp\left[-\left({}^{x}/_{\lambda_{th}}\right)^{n_{th}}\right] \quad (1)$$

where λ_{th} is the characteristic decay length scale of deposit thinning (km), θ_{th} is a thickness scale (cm), and n_{th} is a dimensionless shape parameter. The volume of the deposit is:

$$V = \frac{2\theta_{th}{\lambda_{th}}^2}{n_{th}} \quad (2)$$

The method of Nathenson (2017), which updates Pyle (1989) and Fierstein and Nathenson (1992), calculates deposit volume based on exponential thinning. For the assumption of exponential thinning with a single line segment, thickness varies as:

$$T = T_0\exp\left(-k{A}^{1}/_{2}\right) \quad (3)$$

where T_0 is the maximum thickness (cm), A is the isopach area (km^2), and $-k$ is the slope of the line on a semi-log plot of area$^{1/2}$ vs. deposit thickness. The volume of a deposit based on exponential best-fit is:

$$V = 2T_0/k^2 \quad (4)$$

Finally, the method of Bonadonna and Houghton (2005) calculates the volume of the deposit based on power-law fitting, which is expressed as:

$$T = T_{pl}\sqrt{A}^{(-m)} \quad (5)$$

where A is the isopach area (km^2), T_{pl} is the power-law coefficient, and m is the power-law exponent from a semi-log plot of area$^{1/2}$ vs. deposit thickness. The deposit volume based on power-law best-fit is:

$$V = \frac{2T_{pl}}{2-m}\left(C^{(2-m)} - B^{(2-m)}\right) \quad (6)$$

where B and C represent the proximal and the distal integration limit, respectively. B is taken to be the distance of the calculated maximum thickness:

$$B = \left(\frac{T_0}{T_{pl}}\right)^{\left(-\frac{1}{m}\right)} \quad (7)$$

C is chosen as the most distal extent of the deposit. For T1, a distal integration limit ranging from 40 to 50 km was chosen, and for T2 a range of 18–25 km was chosen. These values were based on where thickness projections reached ~1 cm.

Mass eruption rate

We use the semi-empirical formula from Wilson and Walker, (1987):

$$MER_{ww} = \left(\frac{H}{C}\right)^4 \quad (8)$$

where H is plume height (m), C is an empirical factor (236 m $kg^{-1/4}$ $s^{1/4}$), and MER_{ww} is mass eruption rate (kg/s). The updated empirical relation determined by Mastin et al. (2009) using a magma density of 2500 kg/m^3 can be rearranged to:

$$MER_m = 140H^{4.15} \quad (9)$$

where H is plume height (km) and MER_m is mass eruption rate (kg/s) (Mastin, 2014). Finally, we employ the analytical expression from Degruyter and Bonadonna (2012):

$$MER_{db} = \pi\frac{\rho_{a0}}{g'}\left(\frac{\alpha^2\overline{N}}{10.9}H^4 + \frac{\beta^2\overline{N}^2\overline{v}}{6}H^3\right) \quad (10)$$

where ρ_{a0} is the reference density of the surrounding atmosphere (kg m^{-3}), g' is measured in m/s^2 and defined as $g \cdot ((c_0\theta_0 - c_{a0}\theta_{a0})/c_{a0}\theta_{a0})$ where g is the gravitational acceleration, α is the radial entrainment coefficient, $\overline{N}$ is the average buoyancy frequency (s^{-1}), H is the plume height above the vent (m), β is the wind entrainment coefficient, and $\overline{v}$ is the average wind velocity across the plume (m/ s). MER_{db} is mass eruption rate (kg/s). We estimate a near-vent basaltic plume temperature of 1500 K.

Eruption classification

Following Pyle (1989), b_t is defined as the distance over which the thickness of the deposit halves:

$$b_t = (\ln 2)/(k_t) \quad (11)$$

where k_t is the slope of the exponential line on a plot of thickness (cm) vs. distance from the vent (km). Similarly, b_c is defined as the distance over which the maximum clast size halves:

$$b_c = (\ln 2)/(k_c) \quad (12)$$

where k_c is the slope of the exponential line on a plot of maximum clast size (cm) vs. distance from the vent (km). The Pyle (1989) scheme plots b_t against the half-distance ratio, b_c/b_t.

Following Bonadonna and Costa (2013), λ_{th} represents the characteristic decay length scale of deposit thinning (km) and is calculated with Eq. (1) (Section 6.2 above). $\lambda_{Md\phi}$ describes median grain size variation with distance from the vent (km):

$$Md\phi = \theta_{Md\phi}\left({}^{x}/_{\lambda_{Md\phi}}\right)^{n_{Md\phi}-2}\exp\left[-\left({}^{x}/_{\lambda_{Md\phi}}\right)^{n_{Md\phi}}\right] \quad (13)$$

where $Md\phi$ is median grain size in phi expressed in centimeters, and $\theta_{Md\phi}$ and $n_{Md\phi}$ are other associated Weibull parameters (see Eq. (1)). This scheme plots λ_{th} against the ratio $\lambda_{Md\phi}/\lambda_{th}$.

Appendix B. Supplementary data

Supplementary data to this article can be found online at https://doi.org/10.1016/j.jvolgeores.2019.04.011.

References

Alfano, F., Ort, M.H., Pioli, L., Self, S., Hanson, S.L., Roggensack, K., Allison, C.M., Amos, R., Clarke, A.B., 2018. Subplinian monogenetic basaltic eruption of Sunset Crater, Arizona, USA. GSA Bull. https://doi.org/10.1130/B31905.1.

Alibert, C., Michard, A., Albarède, F., 1986. Isotope and trace element geochemistry of Colorado Plateau volcanics. Geochim. Cosmochim. Acta 50, 2735–2750. https://doi.org/10.1016/0016-7037(86)90223-1.

Arvidson, R.E., Mutch, T.A., 1974. Sedimentary patterns in and around craters from the Pinacate volcanic field, Sonora, Mexico: some comparisons with Mars. Geol. Soc. Am. Bull. 85, 99–104. https://doi.org/10.1130/0016-7606(1974)85<99:SPIAAC>2.0.CO;2.

Biass, S., Bonadonna, C., 2014. TOTGS: total grainsize distribution of tephra fallout. https://vhub.org/resources/3297.

Biass, S., Bagheri, G., Bonadonna, C., 2015. A Matlab implementation of the Carey and Sparks (1986) model. http://vhub.org/resources/3922.

Bonadonna, C., Costa, A., 2012. Estimating the volume of tephra deposits: a new simple strategy. Geology 40 (5), 415–418. https://doi.org/10.1130/G32769.

Bonadonna, C., Costa, C., 2013. Plume height, volume, and classification of explosive volcanic eruptions based on the Weibull function. Bull. Volcanol. 75 (742), 1–19. https://doi.org/10.1007/s00445-013-0742-1.

Bonadonna, C., Houghton, B.F., 2005. Total grain-size distribution and volume of tephrafall deposits. Bull. Volcanol. 67 (5), 441–456. https://doi.org/10.1007/s00445-004-0386-2.

Bonadonna, C., Phillips, J.C., 2003. Sedimentation from strong volcanic plumes. J. Geophys. Res. 108 (B7), 1–28. https://doi.org/10.1029/2002JB002034 2340.

Bonadonna, C., Biass, S., Costa, A., 2015. Physical characterization of explosive volcanic eruptions based on tephra deposits: propagation of uncertainties and sensitivity analysis. J. Volcanol. Geotherm. Res. 296, 80–100. https://doi.org/10.1016/j.jvolgeores.2015.03.009.

Bonadonna, C., Cioni, R., Pistolesi, M., Connor, C., Scollo, S., Pioli, L., Rosi, M., 2018. Determiniation of the largest clast sizes of tephra deposits for the characterization of explosive eruptions: a study of the IAVCEI commission on tephra hazard modelling. Bull. Volcanol. 75 (680), 1–15. https://doi.org/10.1007/s00445-012-0680-3.

Budnikov, V.A., Markhinin, Y.K., Ovsyannikov, A.A., 1983. The quantity, distribution and petrochemical features of pyroclastics of the great Tolbachik fissure eruption. In: Fedotov, S.A., Markhinin, Y.K. (Eds.), The Great Tolbachik Fissure Eruption. Cambridge University Press, New York, pp. 41–56.

Carey, S., Sparks, R.S.J., 1986. Quantitative models of the fallout and dispersal of tephra from volcanic eruption columns. Bull. Volcanol. 48, 109–125. https://doi.org/10.1007/BF01046546.

Coltelli, M., Del Carlo, P., Vezzoli, L., 1998. Discovery of a Plinian basaltic eruption of Roman age at Etna volcano, Italy. Geology 26 (12), 1095–1098. https://doi.org/10.1130/0091-7613(1998)026<1095:DOAPBE>2.3.CO;2.

Connor, L.J., Connor, C.B., 2006. Inversion Is the key to dispersion: Understanding eruption dynamics by inverting tephra fallout. In: Mader, H.M., Coles, S.G., Connor, C.B., Connor, L.J. (Eds.), Statistics in Volcanology. The Geological Society, pp. 231–242 https://doi.org/10.1144/IAVCEI001.18.

Constantini, L., Bonadonna, C., Houghton, B.F., Wehrmann, H., 2009. New physical characterization of the Fontana Lapilli basaltic Plinian eruption, Nicaragua. Bull. Volcanol. 71, 337–355. https://doi.org/10.1007/s00445-008-0227-9.

Degruyter, W., Bonadonna, C., 2012. Improving on mass flow rate estimates of volcanic eruptions. Geophys. Res. Lett. 39, L16308 (p. 1–6). https://doi.org/10.1029/2012GL052566.

Di Traglia, F., Cimarelli, C., de Rita, D., Gimeno Torrente, D., 2009. Changing eruptive styles in basaltic explosive volcanism. Examples from Croscat complex scoria cone, Garrotxa Volcanic Field (NE Iberian Peninsula). J. Volcanol. Geotherm. Res. 180, 89–109. https://doi.org/10.1016/j.jvolgeores.2008.10.020.

Ewart, A., Collerson, K.D., Regelous, M., Wendt, J.I., Niu, Y., 1998. Geochemical evolution within the Tonga-Kermadec-Lau Arc-Back-arc systems: the role of varying mantle wedge composition in space and time. J. Petrol. 39 (3), 331–368. https://doi.org/10.1093/petroj/39.3.331.

Fattahi, M., Stokes, S., 2003. Dating volcanic and related sediments by luminescence methods: a review. Earth Sci. Rev. 62, 229–264. https://doi.org/10.1016/S0012-8252(02)00159-9.
Fierstein, J., Nathenson, M., 1992. Another look at the calculation of fallout tephra volumes. Bull. Volcanol. 54 (2), 156–167. https://doi.org/10.1007/BF00278005.
Fritton, J.G., James, D., Leeman, W.P., 1991. Basic magmatism associated with late Cenozoic extension in the western United States: compositional variations in space and time. J. Geophys. Res. 96 (B8), 13,693–13,711. https://doi.org/10.1029/91JB00372.
Genareau, K., Valentine, G.A., Moore, G., Hervig, R.L., 2010. Mechanisms for transitions in eruptive style at a monogenetic scoria cone revealed by microtextural analyses (Lathrop Wells volcano, Nevada, U.S.A.). Bull. Volcanol. 72, 593–607. https://doi.org/10.1007/s00445-010-0345-z.
Gutmann, J.T., 1977. Textures and genesis of the phenocrysts and megacrysts in basaltic lavas from the Pinacate volcanic field. Am. J. Sci. 277, 833–861. https://doi.org/10.2475/ajs.277.7.833.
Gutmann, J.T., 1979. Structure and eruptive cycle of cinder cones in the Pinacate volcanic field and the controls of Strombolian activity. J. Geol. 87, 448–454.
Gutmann, J.T., 2002. Strombolian and effusive activity as precursors to phreatomagmatism: eruptive sequence at maars of the Pinacate volcanic field, Sonora, Mexico. J. Volcanol. Geotherm. Res. 113, 345–356. https://doi.org/10.1016/S0377-0273(01)00265-7.
Gutmann, J.T., 2007. Geologic studies in the Pinacate volcanic field. Journal of the Southwest 49 (2), 189–243. https://doi.org/10.1353/jsw.2007.0004.
Gutmann, J.T., Turrin, B.D., 2006. The age of Crater Elegante, a maar in the Pinacate volcanic field, Sonora, Mexico. Geol. Soc. Am. Abstr. Programs 38 (6), 32.
Gutmann, J.T., Turrin, B.D., Dohrenwend, J.C., 2000. Basaltic rocks from the Pinacate volcanic field yield notably young $^{40}Ar/^{39}Ar$ ages. EOS 81 (4), 33–44. https://doi.org/10.1029/00EO00018.
Harris, A.J.L., Stevenson, D.S., 1997. Magma budgets and steady-state activity of Vulcano and Stromboli. Geophys. Res. Lett. 24 (9), 1043–1046. https://doi.org/10.1029/97GL00861.
Hill, B.E., Connor, C.B., Jarzemba, M.S., La Femina, P.C., Navarro, M., Strauch, W., 1998. 1995 eruptions of Cerro Negro volcano, Nicaragua, and risk assessment for future eruptions. GSA Bull. 110, 123–124. https://doi.org/10.1130/0016-7606(1998)110<1231:EOCNVN>2.3.CO;2.
Houghton, B.F., Wilson, C.J.N., Smith, I.E.M., 1999. Shallow-seated controls on styles of explosive basaltic volcanism: a case study from New Zealand. J. Volcanol. Geotherm. Res. 91, 97–120. https://doi.org/10.1016/S0377-0273(99)00058-X.
Houghton, B.F., Wilson, C.J.N., Del Carlo, P., Coltelli, M., Stable, J.E., Carey, R., 2004. The influence of conduit processes on changes in style of basaltic Plinian eruptions: Tarawera 1886 and Etna 122 BC. J. Volcanol. Geotherm. Res. 137, 1–14. https://doi.org/10.1016/j.jvolgeores.2004.05.009.
Inman, D.L., 1952. Measures for describing the size distribution of sediments. J. Sediment. Petrol. 22 (3), 125–145. https://doi.org/10.1306/D42694DB-2B26-11D7-8648000102C1865D.
Lian, O.B., Roberts, R.G., 2006. Dating the Quaternary: progress in luminescence dating of sediments. Quat. Sci. Rev. 25, 2449–2468. https://doi.org/10.1016/j.quascirev.2005.11.013.
Luhr, J.F., Aranda-Gómez, J.J., Housh, T.B., 1995. San Quintín Volcanic Field, Baja California Norte, México: geology, petrology, and geochemistry. J. Geophys. Res. 100 (B7), 10,353–10,380. https://doi.org/10.1029/95JB00037.
Lutz, T.M., Gutmann, J.T., 1995. An improved method for determining and characterizing alignments of pointlike features and its implications for the Pinacate volcanic field, Sonora, Mexico. J. Geophys. Res. 100 (B9), 659–670. https://doi.org/10.1029/95JB01058.
Lynch, D.J., 1981. Genesis and Geochronology of Alkaline Volcanism in the Pinacate Volcanic Field Northwestern Sonora, Mexico. Dissertation. University of Arizona.
Lynch, D.J., Gutmann, J.T., 1987. Volcanic structures and alkaline rocks in the Pinacate Volcanic Field of Sonora, Mexico. In: Davis, G.H., VandenDolder, E.M. (Eds.), Geological Diversity of Arizona and Its Margins: Excursions to Choice Areas. vol. 5. Arizona Bureau of Geology and Mineral Technology, pp. 309–322.
Lynch, D.J., Musselman, T.E., Gutmann, J.T., Patchett, P.J., 1993. Isotopic evidence for the origin of Cenozoic volcanic rocks in the Pinacate volcanic field, northwestern Mexico. Lithos 29, 295–302. https://doi.org/10.1016/0024-4937(93)90023-6.
Márquez, A., Oyarzun, R., Doblas, M., Verma, S.P., 1999. Alkalic (ocean-island basalt type) and calc-alkalic volcanism in the Mexican volcanic belt: a cast for plume-related magmatism and propagating rifting at an active margin? Geology 27 (1), 51–54. https://doi.org/10.1130/0091-7613(1999)027<0051:AOIBTA>2.3.CO;2.
Mastin, L.G., 2014. Testing the accuracy of a 1-D volcanic plume model in estimating mass eruption rate. J. Geophys. Res. Atmos. 119, 2474–2495. https://doi.org/10.1002/2013JD020604.
Mastin, L.G., Guffanti, M., Servranckx, R., Webley, P., Barsotti, S., Dean, K., Durant, A., Ewert, J.W., Neri, A., Rose, W.I., Schneider, D., Siebert, L., Stunder, B., Swanson, G., Tupper, A., Volentik, A., Waythomas, C.F., 2009. A multidisciplinary effort to assign realistic source parameters to models of volcanic ash-cloud transport and dispersion during eruptions. J. Volcanol. Geotherm. Res. 186, 10–21. https://doi.org/10.1016/j.jvolgeores.2009.01.008.
McFadden, L.D., Wells, S.G., Jercinovich, M.J., 1987. Influences of eolian and pedogenic processes on the origin and evolution of desert pavements. Geology 15, 504–508. https://doi.org/10.1130/0091-7613(1987)15<504:IOEAPP>2.0.CO;2.
McMillan, N.J., Dickin, A.P., Haag, D., 2000. Evolution of magma source regions in the Rio Grande rift, southern New Mexico. GSA Bull. 112 (10), 1582–1593. https://doi.org/10.1130/0016-7606(2000)112<1582:EOMSRI>2.0.CO;2.
Nakagawa, M., Wada, K., Thordarson, T., Wood, C.P., Gamble, J.A., 1999. Petrologic investigations of the 1995 and 1996 eruptions of Ruapehu volcano, New Zealand: formation of discrete and small magma pockets and their intermittent discharge. Bull. Volcanol. 61, 15–31. https://doi-org.ezproxy1.lib.asu.edu/10.1007/s004450050259.
Nathenson, M., 2017. Revised tephra volumes for Cascade Range volcanoes. J. Volcanol. Geotherm. Res. 341, 42–52. https://doi.org/10.1016/j.jvolgeores.2017.04.021.
Németh, K., 2010. Monogenetic volcanic fields: origin, sedimentary record, and relationship with polygenetic volcanism. Geol. Soc. Am. Spec. Pap. 470, 43–66. https://doi.org/10.1130/2010.2470(04).
NOAA-Air Resources Laboratory, d. Eta Data Assimilation System (EDAS40) Archive Informationhttps://www.ready.noaa.gov/edas40.php.
Osman, S., Rossi, E., Bonadonna, C., Frischknecht, C., Andronico, D., Cioni, R., Scollo, S., 2019. Exposure-based risk assessment and emergency management associated with the fallout of large clasts at Mount Etna. Nat. Hazards Earth Syst. Sci. 19, 589–610. https://doi.org/10.5194/nhess-19-589-2019.
Pérez, W., Freundt, A., Kutterolf, S., Schmincke, H.U., 2009. The Masaya Triple Layer: a 2100 year old basaltic multi-episodic Plinian eruption from the Masaya Caldera Complex (Nicaragua). J. Volcanol. Geotherm. Res. 179, 191–205. https://doi.org/10.1016/j.jvolgeores.2008.10.015.
Petrone, C.M., Francalanci, L., Carlson, R.W., Ferrari, L., Conticelli, S., 2003. Unusual coexistence of subduction-related and intraplate-type magmatism: Sr, Nd and Pb isotope and trace element data from the magmatism of the San Pedro-Ceboruco graben (Nayarit, Mexico). Chem. Geol. 193, 1–24. https://doi.org/10.1016/S0009-2541(02)00229-2.
Pioli, L., Erlund, E., Johnson, E., Cashman, K., Wallace, P., Rosi, M., Delgado Granados, H., 2008. Explosive dynamics of violent Strombolian eruptions: the eruption of Parícutin Volcano 1943–1952 (Mexico). Earth Planet. Sci. Lett. 271, 359–368. https://doi.org/10.1016/j.epsl.2008.04.026.
Pioli, L., Azzopardi, B.J., Cashman, K.V., 2009. Controls on the explosivity of scoria cone eruptions: magma segregation at conduit junctions. J. Volcanol. Geotherm. Res. 186, 407–415. https://doi.org/10.1016/j.jvolgeores.2009.07.014.
Pyle, D.M., 1989. The thickness, volume and grainsize of tephra fall deposits. Bull. Volcanol. 51, 1–15. https://doi.org/10.1007/BF01086757.
Rhodes, E.J., 2011. Luminescence dating of sediments over the past 200,000 years. Annu. Rev. Earth Planet. Sci. 39, 461–488. https://doi.org/10.1146/annurev-earth-040610-133425.
Riggs, N.R., Duffield, W.A., 2008. Record of complex scoria cone eruptive activity at Red Mountain, Arizona, USA, and implications for monogenetic mafic volcanoes. J. Volcanol. Geotherm. Res. 178, 763–776. https://doi.org/10.1016/j.jvolgeores.2008.09.004.
Rogers, G., Saunders, A.D., Terrell, D.J., Verma, S.P., Marriner, G.F., 1985. Geochemistry of Holocene volcanic rocks associated with ridge subduction in Baja California, Mexico. Nature 315, 389–392. https://doi-org.ezproxy1.lib.asu.edu/10.1038/315389a0.
Roggensack, K., Hervig, R.L., McKnight, S.B., Williams, S.N., 1997. Explosive basaltic volcanism from Cerro Negro volcano: influences of volatiles on eruptive style. Science 277, 1639–1642. https://doi.org/10.1126/science.277.5332.1639.
Rossi, E., Bonadonna, C., Degruyter, W., 2019. A new strategy for the estimation of plume height from clast dispersal in various atmospheric and eruptive conditions. Earth Planet. Sci. Lett. 505, 1–12. https://doi.org/10.1016/j.epsl.2018.10.007.
Rowland, S.K., Jurado-Chichay, Z.J., Ernst, G., Walker, G.P.L., 2009. Pyroclastic deposits and lava flows from the 1759–1774 eruption of El Jorullo, México: aspects of 'violent Strombolian' activity and comparison with Parícutin. Studies in Volcanology: The Legacy of George Walker. IAVCEI, Special Publications 2, pp. 105–128.
Sable, J.E., Houghton, B.F., Wilson, C.J.N., Carey, R.J., 2006. Complex proximal sedimentation from Plinian plumes: the example of Tarawera 1886. Bull. Volcanol. 69, 89–103. https://doi.org/10.1007/s00445-006-0057-6.
Scott, C.P., Scott, T., Lao-Davila, D.A., Clarke, A.B., Arrowsmith, J.R., Lynch, D., 2018. Photogrammetric Model of the Tecolote Volcano, Pinacate Volcanic Field, Sonora Mexico (Point Cloud [563M Points], Orthophoto [4 cm/pix], and DEM [8 cm/pix]). Distributed by OpenTopography. https://doi.org/10.5069/G9028PFR.
Storey, M., Rogers, G., Saunders, A.D., Terrell, D.J., 1989. San Quintín volcanic field, Baja California, Mexico: 'within-plate' magmatism following ridge subduction. Terra Research 1 (2), 195–202. https://doi.org/10.1111/j.1365-3121.1989.tb00352.x.
Sun, S.S., McDonough, W.F., 1989. Chemical and isotopic systematics of oceanic basalts: implications for mantle composition and processes. In: Sander, A.D., Norry, M.J. (Eds.), Magmatism in the Ocean Basins. Geological Society of London Special Publication. vol. 42, pp. 313–345. https://doi.org/10.1144/GSL.SP.1989.042.01.19.
Turrin, B.D., Gutmann, J.T., Swisher III, C.C., 2008. A 13 ± 3 ka age determination of a tholeiite, Pinacate volcanic field, Mexico, and improved methods for $^{40}Ar/^{39}Ar$ dating of young basaltic rocks. J. Volcanol. Geotherm. Res. 177, 848–856. https://doi.org/10.1016/j.jvolgeores.2008.01.049.
Valentine, G.A., Gregg, T.K.P., 2008. Continental basaltic volcanoes – processes and problems. J. Volcanol. Geotherm. Res. 177, 857–873. https://doi.org/10.1016/j.jvolgeores.2008.01.050.
Valentine, G.A., Perry, F.V., Krier, D., Keating, G.N., Kelley, R.E., Cogbill, A.H., 2006. Small-volume basaltic volcanoes: eruptive products and processes, and posteruptive geomorphic evolution in Crater Flat (Pleistocene), Southern Nevada. GSA Bull. 118 (11/12), 1313–1330. https://doi.org/10.1130/B25956.1.
Valentine, G.A., Krier, D.J., Perry, F.V., Heiken, G., 2007. Eruptive and geomorphic processes at the Lathrop Wells scoria cone volcano. J. Volcanol. Geotherm. Res. 161, 57–80. https://doi.org/10.1016/j.jvolgeores.2006.11.003.
Valentine, G.A., Cortés, J.A., Widom, E., Smith, E.I., Rasoazanamparany, C., Johnsen, R., Briner, J.P., Harp, A.G., Turrin, B., 2017. Lunar Crater volcanic field (Reveille and Pancake Ranges, Basin and Range Province, Nevada, USA). Geosphere 13 (2), 391–438. https://doi.org/10.1130/GES01428.1.

Vidal-Solano, J.R., Demant, A., Paz Moreno, F.A., Lapierre, H., Ortega-Rivera, M.A., J.K.W, 2008. Insights into the tectonomagmatic evolution of NW Mexico: geochronology and geochemistry of the Miocene volcanic rocks from the Pinacate area, Sonora. GSA Bull., 120, 5/6, p. 691–708. doi:https://doi.org/10.1130/B26053.1.

Walker, G.P.L., 1971. Grain-size characteristics of pyroclastic deposits. J. Geol. 79 (6), 696–714. https://doi.org/10.1086/627699.

Walker, G.P.L., 1973. Explosive volcanic eruptions – a new classification scheme. Geol. Rundsch. 62 (2), 431–446. https://doi.org/10.1007/BF01840108.

Walker, G.P.L., 2000. Basaltic volcanoes and volcanic systems. In: Sigurdsson, H., Houghton, B.F., McNutt, S.R., Rymer, H., Stix, J. (Eds.), Encyclopedia of Volcanoes. Academic Press, San Diego, pp. 683–694.

Walker, G.P.L., Self, S., Wilson, L., 1984. Tarawera 1886, New Zealand – a basaltic Plinian fissure eruption. J. Volcanol. Geotherm. Res. 21, 61–78. https://doi.org/10.1016/0377-0273(84)90016-7.

Williams, S., 1983. Plinian airfall deposits of basaltic composition. Geology 11, 211–214. https://doi.org/10.1130/0091-7613(1983)11<211:PADOBC>2.0.CO;2.

Wilson, L., 1980. Relationships between pressure, volatile content and ejecta velocity in three types of volcanic explosion. J. Volcanol. Geotherm. Res. 8 (2–4), 297–313. https://doi.org/10.1016/0377-0273(80)90110-9.

Wilson, L., Walker, G.P.L., 1987. Explosive volcanic eruptions - VI. Ejecta dispersal in plinian eruptions: the control of eruption conditions and atmospheric properties. Geophys. J. Int. 89 (2), 657–679. https://doi.org/10.1111/j.1365-246X.1987.tb05186.x.